ELSEVIER

Contents lists available at ScienceDirect

# Journal of Sound and Vibration

journal homepage: www.elsevier.com/locate/jsv



# Post-grazing dynamics of a vibro-impacting energy generator



Larissa Serdukova<sup>a,\*</sup>, Rachel Kuske<sup>a</sup>, Daniil Yurchenko<sup>b</sup>

- <sup>a</sup> School of Mathematics, Georgia Institute of Technology, Atlanta, USA
- b IMPEE, Heriot-Watt University, Edinburgh, UK

#### ARTICLE INFO

Article history:
Received 5 February 2020
Revised 26 August 2020
Accepted 22 October 2020
Available online 23 October 2020

PACS: 05.45.-A 43.20.Tb 84.60.-H 85.50.-N

Keywords:
Energy harvesting
Vibro-impact system
Output voltage
Grazing bifurcation
Periodic solutions
Non-smooth dynamics

#### ABSTRACT

The motion of a forced vibro-impacting inclined energy harvester is investigated in parameter regimes with asymmetry in the number of impacts on the bottom and top of the device. This motion occurs beyond a grazing bifurcation, at which alternating top and bottom impacts are supplemented by a zero velocity impact with the bottom of the device. For periodic forcing, we obtain semi-analytical expressions for the asymmetric periodic motion with a ratio of 2:1 for the impacts on the device bottom and top, respectively. These expressions are derived via a set of nonlinear maps between different pairs of impacts, combined with impact conditions that provide jump discontinuities in the velocity. Bifurcation diagrams for the analytical solutions are complemented by a linear stability analysis around the 2:1 asymmetric periodic solutions, and are validated numerically. For smaller incline angles, a second grazing bifurcation is numerically detected, leading to a 3:1 asymmetry. For larger incline angles, period doubling bifurcations precede grazing bifurcations. The converted electrical energy per impact is reduced for the asymmetric motions, and therefore less desirable under this metric.

© 2020 Elsevier Ltd. All rights reserved.

## 1. Introduction

Energy Harvesting (EH) from ambient vibrations was proposed almost two decades ago as an attractive alternative to power supplies or as renewable sources of energy for rechargeable batteries. Since then the gaps in the linear theory of EH have been filled with different methods of energy conversion, based on single-degree-of freedom, multi-degree-of freedom and/or continuous (rods and beams) linear systems on the nano [1], micro [2] and macro scales [3–5]. The excitement regarding the potential of linear EH systems has significantly decreased since then, due to low energy densities of the linear devices, narrow bandwidth and high natural frequency in nano- and micro-scale systems, which are difficult to match in many practical applications. These and other adverse factors lead to insufficient output necessary to power or recharge a battery. The deficiencies in the development of linear EH devices has slowed the proliferation of wireless sensors, particularly critical in the Internet of Things paradigm.

The above limitations in the linear theory of EH have motivated wide-spread efforts on parametrically excited [6–8], nonlinear [9–11] and non-smooth systems. The idea behind parametrically excited systems is the use of large system responses near instabilities, e.g. see [12–15], among others. Within the huge range of nonlinear EH systems [16–18], there are some particular themes of note; natural single-potential nonlinearities (classical continuous nonlinear systems like the

E-mail address: larissa.serdukova@gmail.com (L. Serdukova).

<sup>\*</sup> Corresponding author.

Van-der-Pol oscillator, Lingala et al. [19], Duffing oscillator, Ghouli et al. [20], Zhu [21], Sebald et al. [22], the pendulum, etc.), natural or imposed geometrical nonlinearities (systems with double [23–25], triple [26–28] or multiple stable equilibriums [29,30]), systems with a nonlinear interaction such as flow-induced vibration systems (see [31–36] and references therein), and systems with strongly nonlinear or discontinuous nonlinearities like dry friction, piecewise discontinuity or vibroimpacts [37,38]. It has been shown that the nonlinear mechanisms for EH are far more beneficial than linear ones. This observation follows from the typical structure of the response amplitude vs. forcing frequency or backbone curve, showing a wider bandwidth with higher response amplitude away from a main resonance frequency. However, the design and optimization of a nonlinear energy harvester is far more complex, with limited explicit analytical results, thus requiring extensive complementary experiments or numerics. The available approximation techniques can estimate the response within only a narrow range of parameters imposed by the mathematical assumptions necessary for the applied averaging procedure, typically based on a weakly nonlinear model with small forcing.

Vibro-impact systems have rich phenomenological behaviors, manifesting a variety of routes to nonlinear phenomena like bifurcations, grazing and chaos [39–42]. These effects have been studied in deterministic [43–46] and stochastic vibro-impact systems [47–49]. The models of vibro-impact systems include piecewise linear stiffness [50,51] as well as rigid barriers for instantaneous impacts leading to a velocity jump for inelastic impacts. EH devices that utilize vibro-impact dynamics as a main energy absorption mechanism were developed and studied in a number of publications [52–55]. Other interesting applications of vibro-impact systems include propulsion mechanisms, where the internal impacts are designed to drive the entire system forward or backward. Such systems can be used for autonomous robots and medical devices [56]. While often the study of such systems is limited to computational results only, certain settings allow an analytical or semi-analytical treatment when the motion is composed of a sequence of trajectories described (semi-)analytically. Such an approach translates the piece-wise continuous behavior into a sequence of maps, amenable to analytical treatment [57] that provides explicit parametric expressions for a simple periodic motion. This methodology has certain benefits since it allows bifurcation and stability analyses of various periodic regimes that may occur in the system. Of course, for more complex motions a larger series of maps is necessary, making this particular derivation more tedious and cumbersome.

Recently, Yurchenko et al. [58] proposed a novel vibro-impact energy harvesting (VI-EH) device utilizing dielectric elastomeric (DE) membranes. There it was shown that the performance of such VI-EH depends strongly on the relationship between the excitation and device parameters, leading to various vibro-impact regimes with a low or high power output. The device consists of a forced cylinder with a ball moving freely inside of it, impacting DE membranes covering both ends of the cylinder. Each membrane is composed of the DE material sandwiched between two compliant electrodes, acting as a variable capacitance capacitor. The impacts of the DE membrane by the ball influence its motion while deforming the membrane, leading to energy harvesting via the properties of variable capacitance. The analytical results of [59] gave parametric conditions for a simple periodic motion, consisting of two alternating bottom and top impacts per forcing period. Building on the method of [57], these results considered the asymmetric case of the inclined VI-EH device, providing explicit expressions for impact velocity, phase shift of impact relative to the oscillatory forcing, and time between impacts, in terms of parameters such as the length of the cylinder, excitation parameters, and incline angle. Furthermore, the linear stability of this periodic motion demonstrates the range of parameters where it influences the corresponding VI-EH power output. However, this study did not consider adjacent parameter regimes where more complex periodic motions, period doubling bifurcations, and chaotic motion were observed numerically.

Here we consider a broader class of periodic motions of the VI-EH, referred to here as n:m/pT, where n and m are the number of impacts on the bottom and top membrane, respectively, per period T of the excitation, and p is the ratio of the period of the motion of the VI-EH to T. Then, the motion studied in Serdukova et al. [59] is 1:1/1T motion. Throughout this paper we mainly focus on motions where p=1, as these types of solutions appear over significant parameter ranges when the cylinder is inclined. For convenience of notation, throughout we do not include pT when p=1, and include pT only if p>1.

The goal of this paper is to address a number of problems that have received limited attention for impacting systems of this type. We develop a generalized semi-analytical approach for analysis of n:1 periodic behavior, applied explicitly to the 2:1 case. This approach is particularly valuable in cases when the transition to n:1 motion follows more complex solutions appearing from period doubling or chaotic behavior. By using the maps to develop a series of expressions for a single impact velocity within the periodic solution, it is straightforward to generalize to other types of periodic solutions. This result moves beyond previous results in Luo and Guo [57]and [59], as the generalized approach avoids the cumbersome calculations used to get explicit expressions in those studies. These analytical results provide the basis for our stability analyses of 2:1 solutions and for the comparison of the energy output for 1:1 and 2:1 motions. The comparisons with computations reveal additional unexplored phenomena, not previously documented in the dynamics of such a system: bistability of 2:1 motion and 3:1 motion, with two different types of transitions between these behaviors. While we postpone a full analytical treatment of this bi-stability to future work, the results of this paper illustrate the importance of different types of bifurcations on the energy efficiency of the VI-EH. Thus our analysis here provides a necessary foundation for parametric comparisons between these different types of bifurcations, and for their impact on the energy output.

The paper is organized as follows. A mechanical model and equations of motion of the VI-EH are described in Section 2, together with a review of results from [59] for 1:1 behavior, presented within the larger context of new results from this paper. In Section 3 we outline a semi-analytical method for obtaining parametric conditions for general n:1 periodic solutions, illustrating this method for 2:1 periodic motion. Specifically the results are derived through three nonlinear maps,

corresponding to the three impacts per period, combined with the impact conditions. A linear stability analysis for this motion is given in Section 4, and contrasted with additional routes to grazing behavior. The voltage output of the 2:1 periodic motion is shown in Section 5 and compared with that for the 1:1 periodic motion, together with comparisons of different metrics for the average energy available for harvesting. Finally, conclusions are drawn together with recommendations for the device design.

#### 2. Dynamical model of the vibro-impacting energy harvester

The focus of this paper is a nonlinear vibro-impact energy harvesting device comprised of an externally forced capsule with a freely moving ball inside. Each end of the capsule is closed by a membrane of DE material with compliant electrodes. The friction between the ball and the capsule is neglected, so that the motion of the ball is driven purely through impacts with one of the DE membranes and by gravity. The impact of the ball with the DE membrane not only excites the ball but also causes the DE membrane deformation. Since the DE membrane works as a variable capacitance capacitor, under the deformation its capacitance increases and at the maximum deformation a bias voltage is applied. After the impact, the membrane goes back to its undeformed state and at that point the gained voltage is harvested. The equations of motion for the inclined VI-EH with two DE membranes for harvesting energy from ambient vibrations as developed in Yurchenko et al. [58], as shown in the schematic of Fig. 1.

The cylinder of mass M and length s is subject to a harmonic excitation  $\hat{F}(\omega \tau + \varphi)$  with period  $2\pi/\omega$ . Then the position of its center  $X(\tau)$  satisfies

$$\frac{d^2X}{d\tau^2} = \frac{\hat{F}(\omega\tau + \varphi)}{M}.\tag{1}$$

Between impacts, the ball of mass m ( $M \gg m$ ) rolls freely inside of the cylinder driven only by gravity ( $g = 9.8 \text{ m/s}^2$  is the gravitational constant), with position x given by

$$\frac{d^2x}{d\tau^2} = -G = -g\sin\beta,\tag{2}$$

until it collides with one of the membranes causing its deformation. Since the impact time is negligible with respect to all other time constants in the system, we use an instantaneous impact model in terms of the restitution coefficient r of the membrane. The velocity of the ball changes in sign and magnitude according to [58]

$$\left(\frac{dx}{d\tau}\right)^{+} = \frac{m - rM}{m + M} \left(\frac{dx}{d\tau}\right)^{-} + \frac{M + rM}{m + M} \left(\frac{dX}{d\tau}\right). \tag{3}$$

Superscripts  $\bar{}$  and  $\bar{}$  indicate the velocities of the ball just before and after each impact, respectively. We assume that the velocity of the cylinder  $\dot{X}$  does not change with an impact for m negligible relative to M, so that we drop m in (3) leading to

$$\left(\frac{dx}{d\tau}\right)^{+} = -r\left(\frac{dx}{d\tau}\right)^{-} + (1+r)\left(\frac{dX}{d\tau}\right). \tag{4}$$

In this paper an inelastic impact is considered (r < 1), with most results given for r = 0.5.

To track the dependence of periodic behavior in terms of the parameters, it is valuable to use dimensionless equations of motion in terms of the relative variables. For this purpose we non-dimensionalize the original system (1), (2) with the substitutions

$$X(\tau) = \frac{\parallel \hat{F} \parallel \pi^2}{M\omega^2} \cdot X^*(t), \quad \frac{dX}{d\tau} = \frac{\parallel \hat{F} \parallel \pi}{M\omega} \cdot \dot{X}^*(t), \quad \tau = \frac{\pi}{\omega} \cdot t,$$
 (5)

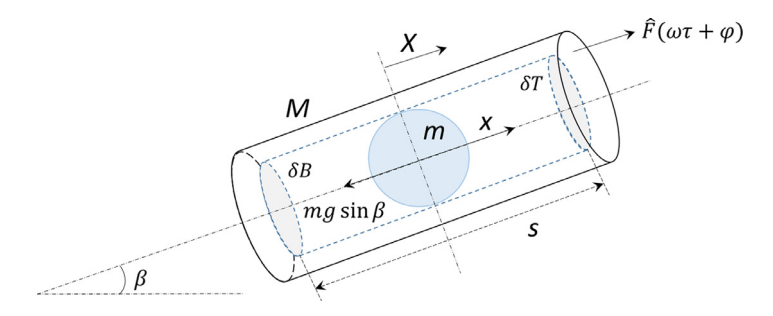


Fig. 1. A mechanical model of a vibro-impact energy harvester adapted from [58].

where  $\|\hat{F}\|$  is an appropriately defined norm of the strength of the forcing  $\hat{F}$  and " " indicates the derivative with respect to t. Then the dimensionless equations of motion in terms of the relative position Z(t) and velocity  $\dot{Z}(t)$  are

$$Z = X^* - x^*, \qquad \dot{Z} = \dot{X}^* - \dot{x}^*$$

$$\ddot{Z} = \ddot{X}^* - \ddot{x}^* = F(\pi t + \varphi) + \frac{Mg \sin \beta}{\|\hat{F}\|} = f(t) + \bar{g},$$
(6)

where the non-dimensional forcing F has the unit norm, i.e. ||F|| = 1, and period 2. Then the impact condition (3) in terms of the non-dimensional relative variables for the j-th impact at time  $t = t_j$  is

$$Z_{j} = X^{*}(t_{j}) - x^{*}(t_{j}) = \pm \frac{d}{2}, \quad \text{for } x \in \partial B \ (\partial T) \text{ the sign is } + (-)$$

$$\dot{Z}_{j}^{+} = -r\dot{Z}_{j}^{-}, \qquad d = \frac{sM\omega^{2}}{\|\hat{F}\| \pi^{2}}, \tag{7}$$

where  $\partial B$  and  $\partial T$  are the bottom and top membranes of the energy harvesting system. Since the dimensionless length of the cylinder d includes a set of four dimensional parameters of the system  $s,M,\omega$  and  $\|\hat{F}\|$ , we focus our analysis primarily on different combinations of two parameters  $\beta$  and d in order to capture the influence of device length, forcing strength, and angle of incline.

### 2.1. Representation of periodic motion with maps

By integrating (6) for  $t \in (t_j, t_{j+1})$  and applying (7), we obtain the expressions for the relative velocity and displacement between two impacts

$$\dot{Z}(t) = -r\dot{Z}_{i}^{-} + \bar{g}(t - t_{j}) + F_{1}(t) - F_{1}(t_{j}), \tag{8}$$

$$Z(t) = Z_j^- - r\dot{Z}_j^-(t - t_j) + \frac{\bar{g}}{2}(t - t_j)^2 + F_2(t) - F_2(t_j) - F_1(t_j)(t - t_j), \tag{9}$$

where  $F_1(t) = \int f(t)dt$  and  $F_2(t) = \int F_1(t)dt$ . In the following expressions, the superscripts " - " are omitted, since (8) and (9) are in terms  $Z^-$  and  $\dot{Z}^-$  only. Evaluating (8) and (9) at impact times  $t = t_{j+1}$ , we obtain equations defining the four basic nonlinear maps  $P_l$ , l = 1, 2, 3, 4 for the corresponding transitions between impacts,

$$P_{1} : (Z_{j} \in \partial B, \dot{Z}_{j}, t_{j}) \mapsto (Z_{j+1} \in \partial B, \dot{Z}_{j+1}, t_{j+1}),$$

$$P_{2} : (Z_{j} \in \partial B, \dot{Z}_{j}, t_{j}) \mapsto (Z_{j+1} \in \partial T, \dot{Z}_{j+1}, t_{j+1}),$$

$$P_{3} : (Z_{j} \in \partial T, \dot{Z}_{j}, t_{j}) \mapsto (Z_{j+1} \in \partial B, \dot{Z}_{j+1}, t_{j+1}),$$

$$(10)$$

and similarly, for  $P_4$  for the  $\partial T \mapsto \partial T$  transition. Here we restrict our attention to  $P_1, P_2$  and  $P_3$  transitions, since only these play a role in the attracting 2:1 motion, as considered in Section 3. The mathematical expressions for these maps take different forms depending on whether  $Z_j$  and  $Z_{j+1}$  are located on either  $\partial B$  or  $\partial T$ . Specifically, for  $t = t_{j+1}$ ,(8) and (9) are given by

$$\dot{Z}_{j+1} = -r\dot{Z}_j + \bar{g}(t_{j+1} - t_j) + F_1(t_{j+1}) - F_1(t_j), \tag{11}$$

$$D_{\ell} = -r\dot{Z}_{j}(t_{j+1} - t_{j}) + \frac{\bar{g}}{2}(t_{j+1} - t_{j})^{2} + F_{2}(t_{j+1}) - F_{2}(t_{j}) - F_{1}(t_{j})(t_{j+1} - t_{j}), \tag{12}$$

where  $D_1 = D_4 = 0, D_2 = -d$  and  $D_3 = d$ .

In [59], the expressions (11) and (12) for the maps  $P_2$  and  $P_3$  over the time intervals  $(t_{k-1}, t_k)$  and  $(t_k, t_{k+1})$  are combined with periodic and impact conditions to derive equations for the triples  $(\dot{Z}_k, \varphi_k, \Delta t_k)$  corresponding to 1:1 periodic solutions. Throughout this paper  $\Delta t_k = t_k - t_{k-1}$  for any k, and  $\varphi_k = \text{mod}(\pi t_k + \varphi, 2\pi)$  is the phase shift of the  $k^{\text{th}}$  impact relative to that of the forcing f(t). The explicit expressions for the triples  $(\dot{Z}_k, \varphi_k, \Delta t_k)$  provide the dependence of 1:1 motion on the combination of the parameters  $d, r, \tilde{g}$  and  $\hat{F}$ .

In Fig. 2(a) and (c) we show the analytical and numerical results for the relative velocity at impact  $\dot{Z}_k$  vs. d for the 1:1 periodic motion based on the results from [59]. The analytical results shown for the 2:1 motion are obtained in Sections 3 and 4 below, where we restrict our analysis to the derivation of the 2:1 solutions and their linear stability. Numerical results are compared to these analytical results for the 2:1 periodic motion, and they also provide branches corresponding to period doubled solutions and chaotic behavior. For decreasing values of d, the 1:1 motion loses stability via a sequence of period doubling bifurcations to 1:1/2T, 1:1/4T, etc. Eventually, for some parameter combinations, an apparently chaotic motion is observed for a window of values of d. For smaller values of d these 1:1/pT with p > 1 or chaotic motions are displaced by asymmetric motions with multiple impacts of  $\partial B$  per period d. Specifically, there is a transition to 2:1 motion at the value  $d = d_{\text{graz}}$ , discussed further in the context of Fig. 4 below. From Fig. 2 we see that 2:1 and other d of d of d of d of d of d of d follow from decreasing d. In the top row, the decreasing values of d follow from decreasing d, while in the bottom

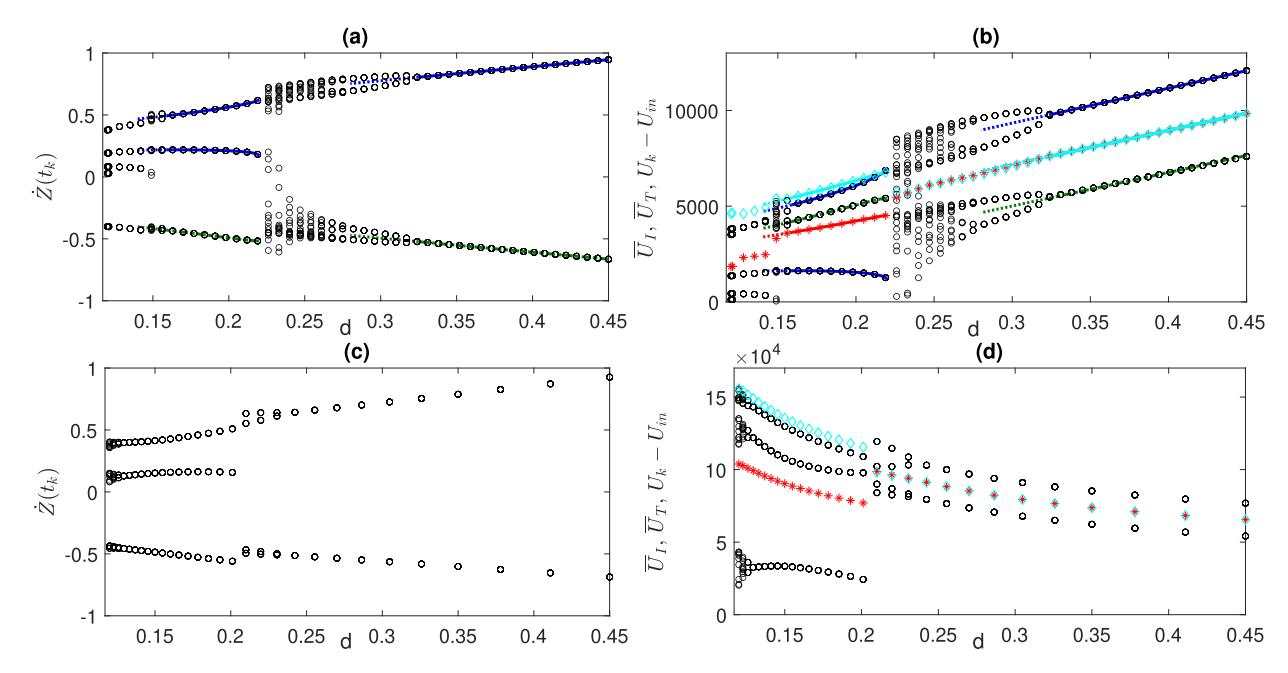
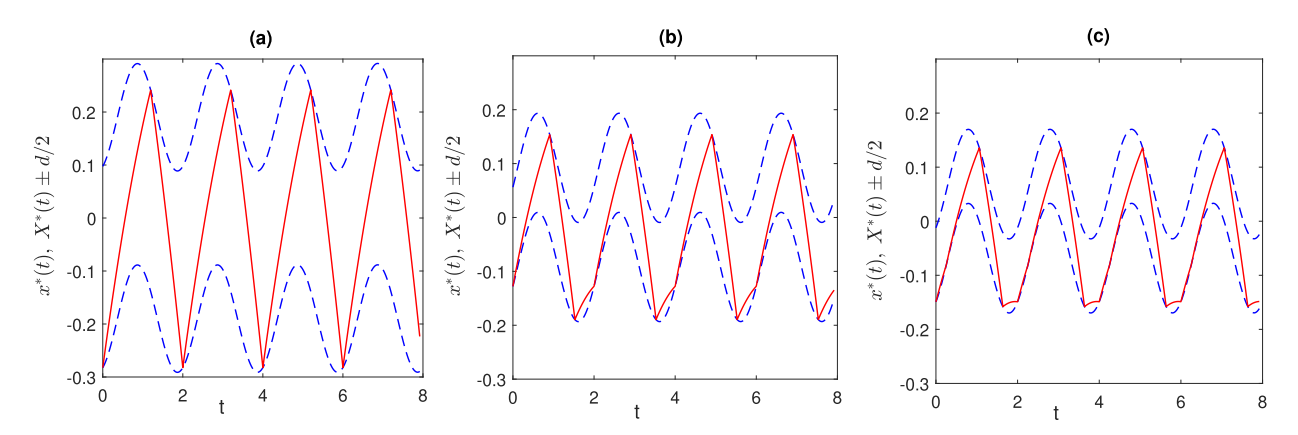


Fig. 2. Numerical (open circles o's, stars \*'s, diamonds  $\diamond$ 's) and analytical stable/unstable (solid, dash-dotted/dashed lines) values for impact velocities and output voltages for  $\beta = \pi/3$  and r = 0.5. (a) Impact velocities (blue solid/green dash-dotted lines for bottom/top) for 0.19 < s < 0.72 m,  $\|\hat{F}\| = 5$  N. The branches for the 2:1 solutions give, from top to bottom,  $\hat{Z}$  following the  $P_3$ ,  $P_1$ ,  $P_2$  transitions. (b) Output voltage  $U_k - U_{\rm in}$  and average value of output voltage per impact  $\overline{U}_I$  (red stars) and per unit time  $\overline{U}_I$  (cyan diamonds) corresponding to  $\hat{Z}$  in (a). The branches for the 2:1 solutions give, from top to bottom,  $U_k$  following the  $P_3$ ,  $P_2$ ,  $P_1$  transitions; (c) and (d) Impact velocity and output voltage for s = 0.85 m with varying  $\|\hat{F}\|$  between 6 N and 22 N. (For interpretation of the references to color in this figure legend, the reader is referred to the web version of this article.)



**Fig. 3.** Time series of the period-T(T=2) absolute displacement of the capsule top and bottom  $X^*(t) \pm d/2$  (blue dashed lines) and the absolute ball displacement  $x^*(t)$  (red solid line) for  $t_0=0$  and  $Z(t_0)=d/2$ . (a) 1:1 motion for d=0.38, s=0.61 m,  $\dot{Z}(t_0)=0.8673$ ,  $\varphi=0.4217$ ; (b) 2:1 motion for d=0.184, s=0.30 m,  $\dot{Z}(t_0)=0.2164$ ,  $\varphi=1.21$ ; (c) 3:1 motion for d=0.137, s=0.22 m,  $\dot{Z}(t_0)=0.2059$ ,  $\varphi=0.6503$ . For all figures M=124.5g, r=0.5 and  $\omega=5\pi$  Hz. (For interpretation of the references to color in this figure legend, the reader is referred to the web version of this article.)

row the decreasing d follows from increasing  $\hat{F}$ . To compare the 1:1, 2:1 and 3:1 motions, Fig. 3 shows the absolute displacements  $X^*(t) \pm d/2$  of the top and bottom of the cylinder under an external force and the motion of the ball  $x^*(t)$  in the cylinder, illustrating the number of impacts per period for each case.

In Fig. 2(b) and (d) we show the analytical and numerical results for the output voltage  $U_k - U_{\rm in}$  vs. d for the same range of d as in (a) and (c), respectively. A calculation of the energy output follows directly from  $(\dot{Z}_k, \varphi_k, \Delta t_k)$ , based on the deformation of the membrane that depends explicitly on  $\dot{Z}_k^2$ . Given a constant input voltage,  $U_{\rm in}$ , applied to the membranes, the change in charge Q across the capacitor is given by  $\Delta Q = U \Delta C$ , where C is its capacitance. The charge Q increases as the membrane's shape is restored, producing a higher voltage  $U_k$  at the kth impact, with resulting energy to be harvested in terms of the difference,  $U_k - U_{\rm in}$ , which we refer to as the output voltage.

Two different averaged output voltages are also shown, average per impact  $\overline{U}_I$  and average per time unit  $\overline{U}_T$ , based on 30 (non-dimensionalized) time units in t ( $\tau = 6$  s) for 1:1 motion and 20 time units in t ( $\tau = 4$  s) for 2:1 motion. Note

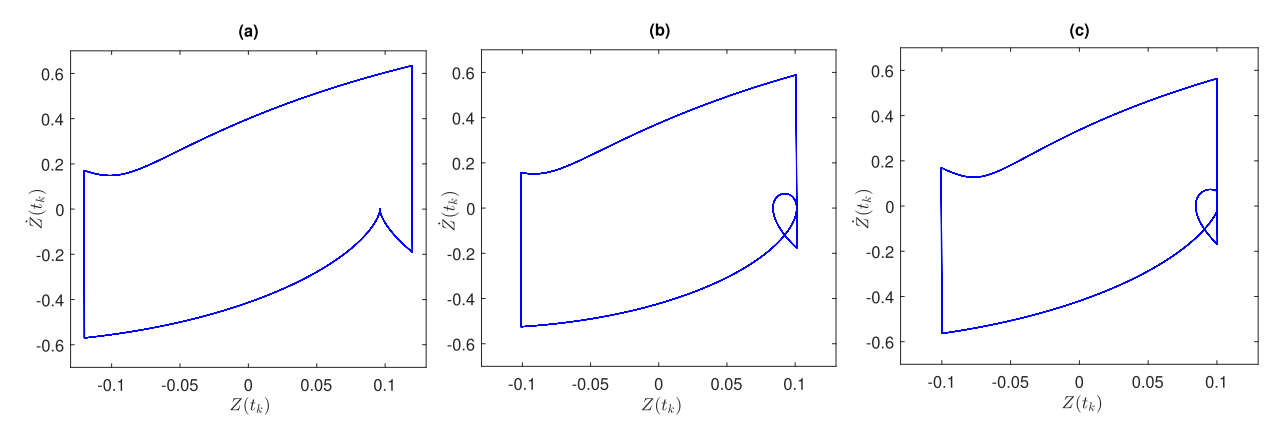


**Fig. 4.** Phase portrait for initial relative position  $Z(t_0) = d/2$ , M = 124.5g, r = 0.3,  $\beta = \pi/18$ ,  $\|\hat{F}\| = 5$ N,  $\omega = 5\pi$  Hz. (a) 1:1 motion with d = 0.24, s = 0.3855 m,  $\dot{Z}(t_0) = 0.6349$ ,  $\varphi = 0.4579$ ; (b) Grazing bifurcation point with d = 0.2025, s = 0.3253 m,  $\dot{Z}(t_0) = 0.5899$ ,  $\varphi = 0.3040$ ; (c) 2:1 motion with d = 0.2008, s = 0.3226 m,  $\dot{Z}(t_0) = 0.5644$ ,  $\varphi = 0.2986$ .

Fig. 4 illustrates the possible transition from 1:1 to 2:1 families of solutions in the phase plane, via a grazing bifurcation at a value of  $d = d_{\text{graz}}$  where  $\dot{Z}_k = 0$  and  $Z_k = d/2$ , shown in Fig. 4(b). Note that the grazing transition from 1:1 to 2:1 motions is shown for r = 0.3 in Fig. 4, in contrast to the transition to 2:1 solutions shown in Fig. 2(a), (c) for r = 0.5, where a series of period doubling bifurcations precedes grazing as d decreases. Preliminary observations suggest that, as d decreases, period doubling bifurcations tend to precede grazing for larger values of r. However, such observations also depend on the angle  $\beta$ . Our focus in this paper is on 2:1 periodic behavior, and the influence of  $\beta$  and d on its appearance. In particular, the complex transition from 1:1 to 2:1 behavior for larger values of r motivates the need for an analytical prediction for the onset of 2:1 solutions, as given in Section 3. There it is shown how the direct calculation of 2:1 solutions from the maps  $P_j$  is clearly preferable to determining grazing conditions from the 1:1/pT or chaotic solutions. The interplay of a range of values of r with the angle  $\beta$  is left for future investigations of period doubling bifurcations, chaotic behavior, and grazing.

# 3. Analytical expressions for periodic 2:1 motion

In this section we obtain analytical expressions for the parametric dependence of the 2:1 motion, using the maps  $P_1, P_2$  and  $P_3$  for the sequence of impacts over the intervals  $\Delta t_j$  for j = k, k + 1, k + 2.

Note that this calculation is a particular application of the general approach for deriving n:1 periodic solutions for (6) and (7). An n:1 periodic solution is composed of n-1 applications of  $P_1$ , followed by  $P_2$  and  $P_3$ . The unknowns needed to define the motion are n+1 values of the impact velocity  $\dot{Z}_{k+\ell}$ ,  $\ell=0\ldots,n$ , the time intervals  $T_\ell$  for the n+1 maps, and the phase difference at impact  $\varphi_k=\operatorname{mod}(\pi t_k+\varphi,2\pi)$ . Then these 2n+3 unknowns are obtained from the Eq. (9) for  $\dot{Z}_{k+\ell}$  and  $Z_{k+\ell}$  for each of the 2(n+1) maps  $P_j$ , and the periodic condition  $\sum_{\ell=1}^{n+1}T_\ell=T$ . The values  $(\dot{Z}_k,\varphi_k,\Delta t_k,\ldots,\Delta t_{k+n-1})$  are determined from n+2 equations for  $\dot{Z}_k$  that can be obtained from a generalizable sequence of steps. These steps are:

- summing the equations for the impact velocities from all the maps  $P_i$ ,
- summing the equations for the relative position at impact from all the maps  $P_j$ ,
- n-1 combinations of successive pairs of equations for impact velocity  $\dot{Z}_{k+j}$  and impact position  $Z_{k+j+1}$ , for  $j=1,\ldots,n-1$ .
- the expression for  $\dot{Z}_k$  given by the equation for the relative position  $Z_{k+1}$  in the initial map  $P_1$ .

Using  $\dot{Z}_{k+n+1} = \dot{Z}_k$  together with these steps, we get n+2 equations of the form  $\dot{Z}_k = h_\ell(\varphi_k, \Delta t_k, \dots, \Delta t_{k+n-1})$ , which can then be solved simultaneously with a numerical algebraic equation solving package. In addition, the remaining  $\dot{Z}_{k+m}$  for

m = 1, ..., n can be obtained from a successive application of the equations for the impact velocities from the successive maps.

Demonstrating this approach for the 2:1 periodic motion, we derive the equations for the quadruples  $(\dot{Z}_k, \varphi_k, \Delta t_k, \Delta t_{k+1})$  corresponding to the 2:1 periodic solutions of (6) and (7), in terms of the parameters d,r and  $\bar{g}$ , with  $\Delta t_k$  and  $\varphi_k = \text{mod}(\pi t_k + \varphi, 2\pi)$  as defined in Section 2. We focus on a 2:1 motion with three impacts per period T of the forcing f(t), so that

$$t_{k+3} = T + t_k$$
,  $Z_k = Z_{k+3}$ , and  $\dot{Z}_{k+3} = \dot{Z}_k$ . (13)

The times for the transitions  $P_1, P_2$  and  $P_3$  are defined as  $T_1, T_2$  and  $T_3$ , with

$$T_1 = \Delta t_k = t_{k+1} - t_k, \quad T_2 = \Delta t_{k+1} = t_{k+2} - t_{k+1},$$

$$T_3 = \Delta t_{k+2} = t_{k+3} - t_{k+2}, \quad T = T_1 + T_2 + T_3.$$
(14)

The 2:1 motion is then described by the three maps  $P_1$ ,  $P_2$  and  $P_3$  from (11) and (12)

$$P_{1} : (Z_{k} \in \partial B, \dot{Z}_{k}, t_{k}) \mapsto (Z_{k+1} \in \partial B, \dot{Z}_{k+1}, t_{k+1}),$$

$$\dot{Z}_{k+1} = -r\dot{Z}_{k} + \bar{g}T_{1} + F_{1}(t_{k+1}) - F_{1}(t_{k}),$$
(15)

$$0 = -r\dot{Z}_k T_1 + \frac{\bar{g}}{2} T_1^2 + F_2(t_{k+1}) - F_2(t_k) - F_1(t_k) T_1.$$
(16)

$$P_{2}: (Z_{k+1} \in \partial B, \dot{Z}_{k+1}, t_{k+1}) \mapsto (Z_{k+2} \in \partial T, \dot{Z}_{k+2}, t_{k+2}),$$

$$\dot{Z}_{k+2} = -r\dot{Z}_{k+1} + \bar{g}T_{2} + F_{1}(t_{k+2}) - F_{1}(t_{k+1}),$$
(17)

$$-d = -r\dot{Z}_{k+1}T_2 + \frac{\bar{g}}{2}T_2^2 + F_2(t_{k+2}) - F_2(t_{k+1}) - F_1(t_{k+1})T_2.$$

$$\tag{18}$$

$$P_{3} : (Z_{k+2} \in \partial T, \dot{Z}_{k+2}, t_{k+2}) \mapsto (Z_{k+3} \in \partial B, \dot{Z}_{k+3}, t_{k+3}),$$

$$\dot{Z}_{k+3} = -r\dot{Z}_{k+2} + \bar{g}T_{3} + F_{1}(t_{k+3}) - F_{1}(t_{k+2}),$$
(19)

$$d = -r\dot{Z}_{k+2}T_3 + \frac{\bar{g}}{2}T_3^2 + F_2(t_{k+3}) - F_2(t_{k+2}) - F_1(t_{k+2})T_3.$$
(20)

We first use a number of substitutions to eliminate  $\dot{Z}_{k+1}, \dot{Z}_{k+2}$  from (15)–(20) and obtain four equations in terms of  $\dot{Z}_k$ , from which we obtain  $(\dot{Z}_k, \varphi_k, \Delta t_k, \Delta t_{k+1})$ .

By adding (15), (17), (19) and using the relationships  $T = T_1 + T_2 + T_3$ , and  $F_1(t_{k+3}) = F_1(T + t_k) = F_1(t_k)$ , we obtain

$$\dot{Z}_k = \frac{1}{1 - r + r^2} \left[ (r - 1)\bar{g}T_1 - \bar{g}T_2 + (1 - r)F_1(t_k) + rF_1(t_{k+1}) - F_1(t_{k+2}) + \frac{T\bar{g}}{r+1} \right]. \tag{21}$$

A second equation for  $\dot{Z}_k$  is obtained from (16)

$$\dot{Z}_k = \frac{1}{rT_1} [F_2(t_{k+1}) - F_2(t_k)] + \frac{1}{2r} [\tilde{g}T_1 - 2F_1(t_k)]. \tag{22}$$

Substituting (15) into (18) yields a third expression for  $\dot{Z}_k$ 

$$\dot{Z}_{k} = \frac{1}{r} [\bar{g}T_{1} + F_{1}(t_{k+1}) - F_{1}(t_{k})] - \frac{1}{r^{2}T_{2}} [d + F_{2}(t_{k+2}) - F_{2}(t_{k+1})] - \frac{1}{2r^{2}} [\bar{g}T_{2} - 2F_{1}(t_{k+1})]. \tag{23}$$

Finally, adding (16), (18), (20) and using relationship  $F_2(t_{k+3}) = F_2(T + t_k) = F_2(t_k)$  gives a fourth equation for  $\dot{Z}_k$ 

$$\dot{Z}_{k} = \frac{1}{r^{3}T_{3} - r^{2}T_{2} + rT_{1}} \left[ \frac{\bar{g}}{2} (T_{1}^{2} + T_{2}^{2} + T_{3}^{2}) + F_{1}(t_{k})(-r^{2}T_{3} + rT_{2} - T_{1}) \right] + 
+ \frac{1}{r^{3}T_{3} - r^{2}T_{2} + rT_{1}} \left[ F_{1}(t_{k+1})(r^{2}T_{3} - rT_{2} + rT_{3} - T_{2}) + r^{2}\bar{g}T_{1}T_{3} - r\bar{g}T_{1}T_{2} \right] + 
+ \frac{1}{r^{3}T_{3} - r^{2}T_{2} + rT_{1}} \left[ -r\bar{g}T_{2}T_{3} - (1 + r)T_{3}F_{1}(t_{k+2}) \right].$$
(24)

Then we solve (21)–(24) to obtain  $(\dot{Z}_k, \varphi_k, \Delta t_k, \Delta t_{k+1})$ , using the Matlab function *vpasolve*. A specific choice of  $f(t) = \cos(\pi t + \varphi)$  for which

$$F_1(t) = \frac{1}{\pi} \sin(\pi t + \varphi) \text{ and } F_2(t) = -\frac{1}{\pi^2} \cos(\pi t + \varphi),$$
 (25)

provides specifics for the equations for  $(\dot{Z}_k, \varphi_k, \Delta t_k, \Delta t_{k+1})$ . It is convenient to write the time intervals between impacts in terms of the parameters q and p, that capture the fractions of the period of forcing corresponding to each of the three impacts as follows,

$$T_1 = 2nq$$
,  $T_2 = 2np$ ,  $T_3 = 2n(1-q-p)$ , and  $T = 2n$ . (26)

We take n=1 for which the period is T=2. Without loss of generality, we take  $t_k=0$ , so  $\varphi_k=\text{mod}(\varphi,2\pi)$ . Then the four Eqs. (21)–(24)take the form of  $\dot{Z}_k$  as functions of  $\varphi,q$ , and p

$$\dot{Z}_{k} = \frac{1}{1 - r + r^{2}} \left[ 2nq(r - 1)\bar{g} - 2np\bar{g} + \frac{1 - r}{\pi} \sin(\pi t_{k} + \varphi) + \frac{r}{\pi} \sin(\pi [t_{k} + 2nq] + \varphi) \right] 
+ \frac{1}{1 - r + r^{2}} \left[ -\frac{1}{\pi} \sin(\pi [t_{k} + 2nq + 2np] + \varphi) + \frac{2n\bar{g}}{r + 1} \right],$$

$$\dot{Z}_{k} = \frac{1}{\pi r} \left[ n\pi q\bar{g} - \sin(\pi t_{k} + \varphi) - \frac{1}{2n\pi q} \cos(\pi [t_{k} + 2nq] + \varphi) + \frac{1}{2n\pi q} \cos(\pi t_{k} + \varphi) \right],$$
(28)

$$\dot{Z}_{k} = \frac{1}{\pi r^{2}} \left[ \sin(\pi [t_{k} + 2nq] + \varphi) + 2n\pi q r \bar{g} + r \sin(\pi [t_{k} + 2nq] + \varphi) - r \sin(\pi t_{k} + \varphi) \right] 
+ \frac{1}{\pi r^{2}} \left[ \frac{1}{2n\pi p} \cos(\pi [t_{k} + 2nq + 2np] + \varphi) - \frac{1}{2n\pi p} \cos(\pi [t_{k} + 2nq] + \varphi) - n\pi p \bar{g} - \frac{\pi d}{2np} \right],$$
(29)

$$\begin{split} \dot{Z}_k &= \frac{\sin(\pi t_k + \varphi)(-2nr^2(1-p-q) + 2npr - 2nq)}{2nr^3(1-p-q) - 2npr^2 + 2nqr} \\ &- \frac{2n\sin(\pi [t_k + 2nq + 2np] + \varphi)(1-p-q)(1+r)}{2n\pi r^3(1-p-q) - 2n\pi pr^2 + 2n\pi qr} \\ &+ \frac{\sin(\pi [t_k + 2nq] + \varphi)(2nr^2(1-p-q) - 2npr + 2nr(1-p-q) - 2np)}{2nr^3(1-p-q) - 2npr^2 + 2nqr} \\ &+ \frac{4n^2r^2\bar{g}q(1-p-q) - 4n^2\bar{g}rpq - 4n^2\bar{g}rp(1-p-q) + \bar{g}(2n^2q^2 + 2n^2p^2 + 2n^2(1-p-q)^2)}{2nr^3(1-p-q) - 2npr^2 + 2nqr}. \end{split}$$

Solving (27)–(30) for varying d, one gets the quadruples  $(\dot{Z}_k, \varphi_k, \Delta t_k, \Delta t_{k+1})$  for 2:1 solutions. Then  $\dot{Z}_{k+1}$  is obtained from (15) and substitution of (15) into (17) gives the equation for  $\dot{Z}_{k+2}$ ,

$$\dot{Z}_{k+2} = r^2 \dot{Z}_k - r\bar{g}T_1 + \bar{g}T_2 + rF_1(t_k) - (1+r)F_1(t_{k+1}) + F_1(t_{k+2}). \tag{31}$$

Fig. 5 shows the analytical solutions for these quadruples for different angles of incline  $\beta$  and compares them to the values obtained from numerical simulations of Eqs. (6) and (7). The analytical results provide the existence of these 2:1 solutions over a range of d, with the largest value of d corresponding to the transition from 1:1/pT or chaotic solutions for decreasing values of d. The stability analysis, provided in the next section, also demonstrates that the 2:1 solutions are stable at these transitions. The stable 2:1 solutions, represented by the solid blue lines (impacts on  $\partial T$ ), agree with the numerical solutions represented by black open circles. The unstable 2:1 solutions represented by dashed lines are also found analytically. The points  $A_1$ ,  $A_2$ ,  $A_3$ , B are the critical points that indicate a change in the type or stability or instability of the 2:1 solutions, based on the linear stability analysis. For larger values of  $\beta$ , as shown for the top three rows in Fig. 5, the solutions lose stability to a period doubling bifurcation as d decreases; specifically, the 2:1 solution is stable in the ranges of 0.169 < d < 0.22 for  $\beta = \pi/2$  in (a)–(c), 0.159 < d < 0.22 for  $\beta = \pi/3$  in (d)–(f), 0.146 < d < 0.213 for  $\beta = \pi/4$  in (g)–(i). Note that the value of d for the period doubling bifurcation d decreases with decreasing d0. A similar trend was observed for 1:1 solutions in Serdukova et al. [59].

For the case of  $\beta = \pi/6$  in the bottom row of Fig. 5, vertical lines indicate the numerically detected grazing bifurcations at  $d = G_1$  and  $d = G_2$ , corresponding to  $Z_j = d/2$  and  $\dot{Z}_j = 0$ . There are two different values, since the bifurcation value differs depending on whether it is obtained from decreasing the parameter d, yielding a transition from a 2:1 solution to a 3:1 solution at  $d = G_1$ , or by increasing d, yielding a transition from 3:1 to 2:1 solutions at  $d = G_2$ . These results indicate a region of bi-stability for the 2:1 and 3:1 solutions, which we discuss briefly in Section 4.2. Here the 2:1 solution is stable in the ranges of 0.1373 < d < 0.206 (j)–(l). Note the lower value on this range corresponds to the grazing bifurcation at  $G_1$ , while the period doubling bifurcation from the linear analysis of the 2:1 solution occurs at d = 0.133 (below  $G_1$ ). The implications of the location of these bifurcations is discussed further in Section 4.2 below.

#### 4. Stability and bifurcation of 2:1 motion

## 4.1. Linear stability analysis

The critical points  $A_j$ , B as shown in Fig. 5 are obtained from a linear stability analysis around the quadruples  $(\dot{Z}_k, \varphi_k, \Delta t_k, \Delta t_{k+1})$  corresponding to the asymmetric period-T solutions. A complete review of this method can be found in Shaw and Holmes [50], Luo and Guo [57], Luo [60].

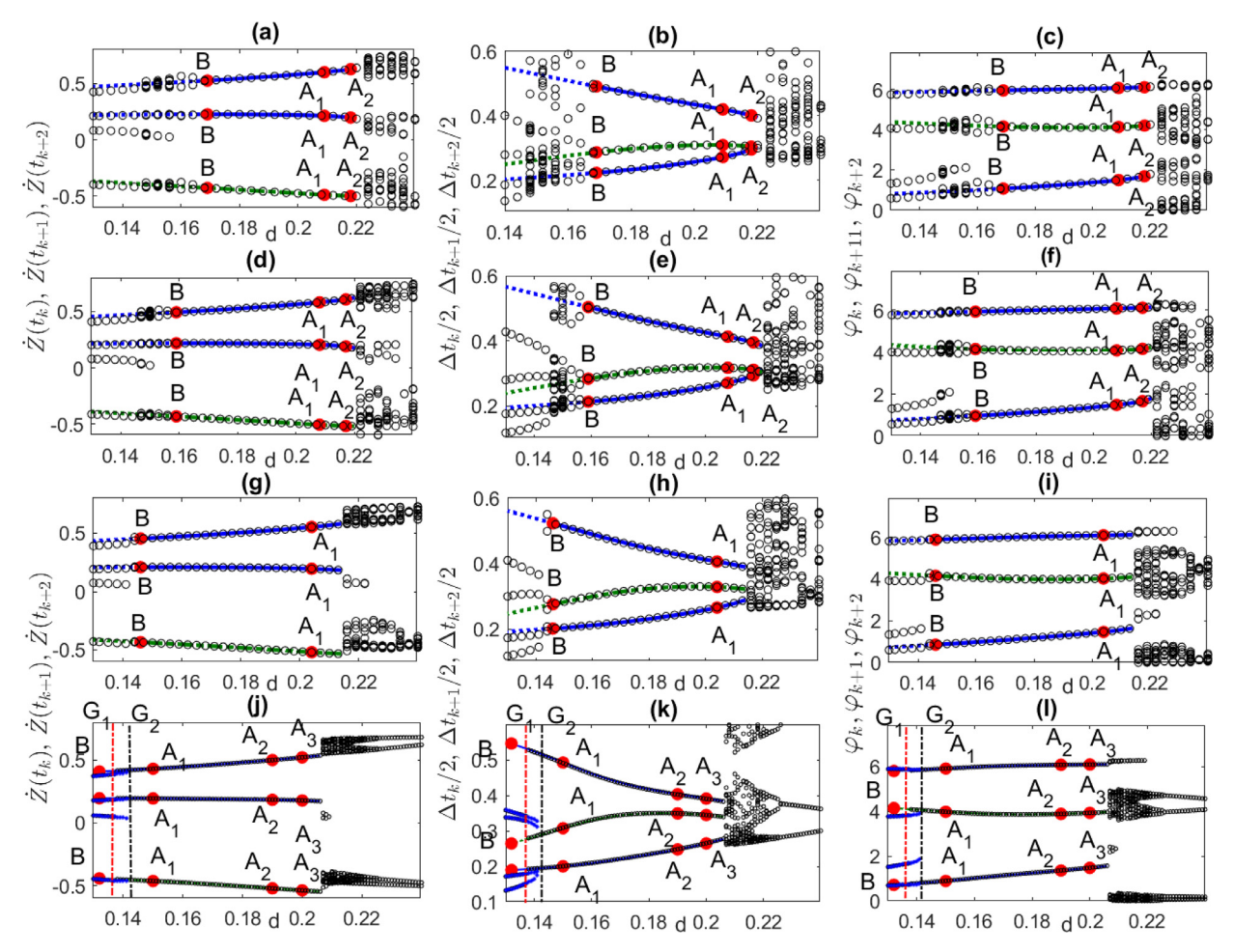


**Fig. 5.** Blue solid and green dash-dotted lines show the analytical results for the 2:1 periodic solutions for 0.2088 < s < 0.3855 m, with numerical results indicated by open circles. Solid and dash-dotted (dashed) lines correspond to stable (unstable) analytical solutions. Red circles labeled as Aj, or B indicate critical points from the linear stability analysis, described in Table 1. (a)–(c) Asymmetric branches of the period-Tsolutions for β = π/2; (d)–(f) Asymmetric branches of the period-Tsolutions for β = π/3; (g)–(i) Asymmetric branches of the period-Tsolutions for β = π/4; (j)–(l) Asymmetric branches of the period-Tsolutions for β = π/4. The vertical lines correspond to grazing bifurcations;  $d = G_1(black)$  ( $d = G_2$  (red)) for the transition from 3:1 to 2:1 (2:1 to 3:1) solutions with increasing (decreasing) d. In panels (a), (d), (g), (j) the branches for the 2:1 solutions give, from top to bottom,  $∂x_i$  at impacts following the  $A_i$ ,  $A_i$ ,  $A_i$  transitions; in panels (b), (e), (h), (k) the branches for the 2:1 solutions give, from top to bottom,  $∂x_i$ ,  $A_i$  transitions. For all figures  $A_i$  transitions in panels (c), (f), (i), (l) the branches for the 2:1 solutions give, from top to bottom,  $A_i$ ,  $A_i$  transitions. For all figures  $A_i$  transitions article.)

Considering a small perturbation  $\delta \mathbf{H}_k$  to the fixed point  $\mathbf{H}_k^* = (t_k, \dot{Z}_k)$ , we obtain the equation for  $\delta \mathbf{H}_{k+3}$  linearized about  $\delta \mathbf{H}_k = 0$ ,

$$\delta \mathbf{H}_{k+3} = DP(\mathbf{H}_{k}^{*})\delta \mathbf{H}_{k} = DP_{3}(\mathbf{H}_{k+2}^{*}) \cdot DP_{2}(\mathbf{H}_{k+1}^{*}) \cdot DP_{1}(\mathbf{H}_{k}^{*}) \delta \mathbf{H}_{k}, \tag{32}$$

with

$$DP = DP_{3} \cdot DP_{2} \cdot DP_{1}$$

$$= \begin{bmatrix} \frac{\partial t_{k+3}}{\partial t_{k+2}} & \frac{\partial t_{k+3}}{\partial \dot{z}_{k+2}} \\ \frac{\partial \dot{z}_{k+3}}{\partial t_{k+2}} & \frac{\partial \dot{z}_{k+3}}{\partial \dot{z}_{k+2}} \end{bmatrix}_{\mathbf{H}_{k+2} = \mathbf{H}_{k+2}^{*}} \cdot \begin{bmatrix} \frac{\partial t_{k+2}}{\partial t_{k+1}} & \frac{\partial t_{k+2}}{\partial \dot{z}_{k+1}} \\ \frac{\partial \dot{z}_{k+2}}{\partial t_{k+1}} & \frac{\partial z_{k+2}}{\partial z_{k+1}} \end{bmatrix}_{\mathbf{H}_{k+1} = \mathbf{H}_{k+1}^{*}} \cdot \begin{bmatrix} \frac{\partial t_{k+1}}{\partial t_{k}} & \frac{\partial t_{k+1}}{\partial \dot{z}_{k}} \\ \frac{\partial \dot{z}_{k+1}}{\partial t_{k}} & \frac{\partial \dot{z}_{k+1}}{\partial \dot{z}_{k}} \end{bmatrix}_{\mathbf{H}_{k} = \mathbf{H}_{k}^{*}}.$$

$$(33)$$

The entries  $\frac{\partial t_{l+1}}{\partial t_l}$ ,  $\frac{\partial t_{l+1}}{\partial z_l}$ ,  $\frac{\partial \dot{z}_{l+1}}{\partial z_l}$ ,  $\frac{\partial \dot{z}_{l+1}}{\partial z_l}$  for l=k,k+1,k+2 are given in Appendix A. Using the trace Tr(DP) (A.4) and determinant Det(DP), the eigenvalues of the matrix DP in (33) are computed by

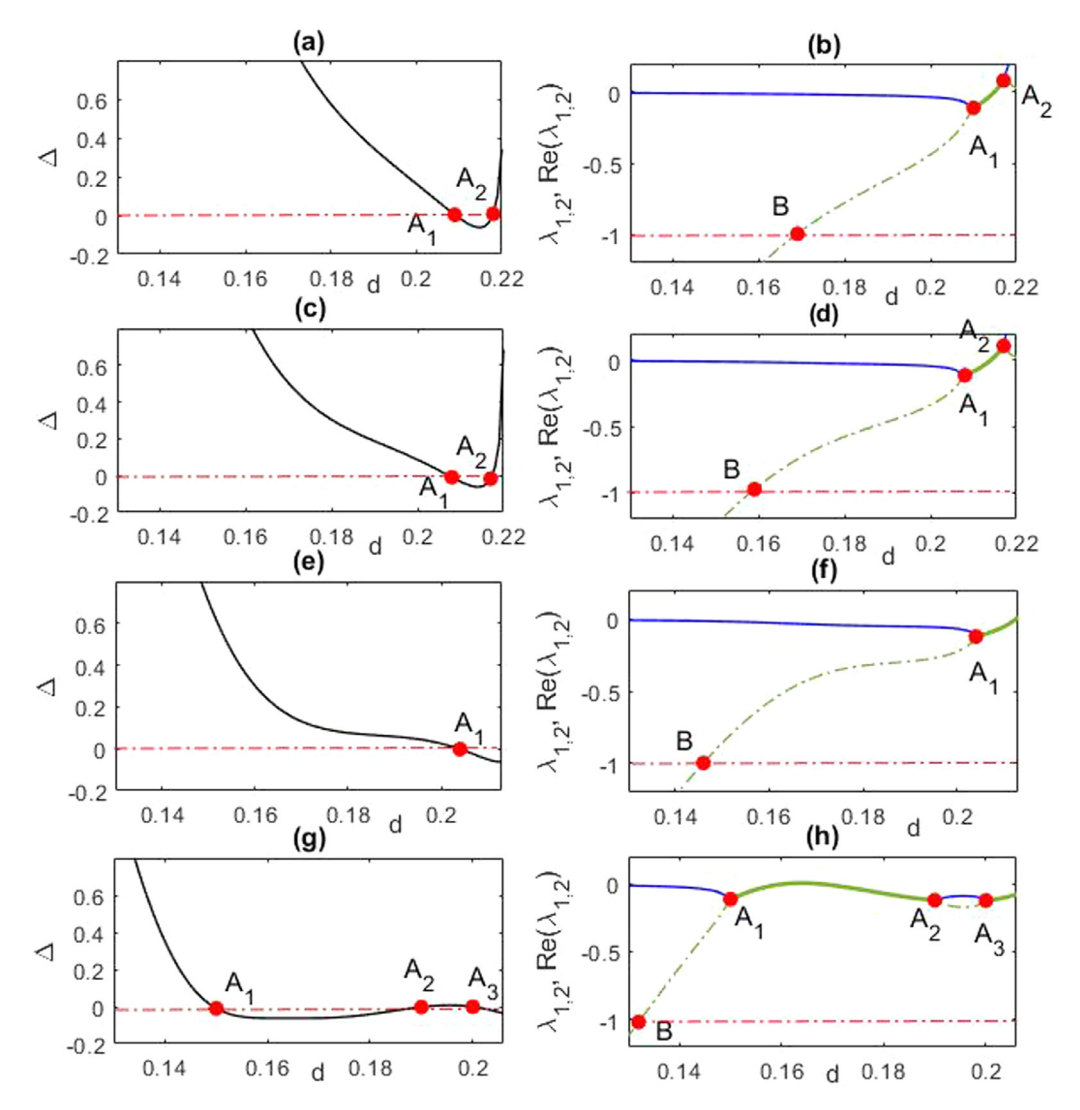


**Fig. 6.** Graphs of  $\Delta$  (left column), and eigenvalues from the linear stability analysis (right column), showing real eigenvalues  $\lambda_{1,2}$  (blue solid and green dash-dotted thin lines) and real part of complex eigenvalues Re $\lambda_{1,2}$  (green thick line) to confirm types and stability of solutions. Red circles labeled as Aj, or B indicate critical points from the linear stability analysis, described in Table 1. In (a) and (b) for  $\beta = \pi/2$ .0.2088 < s < 0.3534 m; in (c) and (d) for  $\beta = \pi/3$  and 0.2088 < s < 0.3534 m; in (e) and (f) for  $\beta = \pi/4$  and 0.2088 < s < 0.3373 m; in (g) and (h) for  $\beta = \pi/6$  and 0.2088 < s < 0.3373 m. The red dot-dashed lines for  $\Delta = 0$  and  $\lambda_{1,2} = -1$  represent boundaries of the stability criteria. The left-most red circle in (h) corresponds to  $\lambda_j = -1$  from the stability analysis. For all figures M = 124.5 g, r = 0.5,  $|| \hat{F} || = 5$ N and  $\omega = 5\pi$  Hz. (For interpretation of the references to color in this figure legend, the reader is referred to the web version of this article.)

$$\lambda_{1,2} = \frac{\operatorname{Tr}(DP) \pm \sqrt{\Delta}}{2},$$

$$\Delta = [\operatorname{Tr}(DP)]^2 - 4\operatorname{Det}(DP),$$
(34)

and shown in Fig. 6. The corresponding stability and analytical bifurcation conditions as obtained from the linear stability analysis are described in Table 1 below.

If  $\Delta < 0$ , as shown for  $d_{A_1} < d < d_{A_2}, d > d_{A_3}$  and in Fig. 6(a), (c), (e), (g), the eigenvalues of the matrix DP are two complex conjugates. Their corresponding real parts  $Re(\lambda_i) = Tr(DP)/2$  are shown in Fig. 6(b), (d), (f), (h), depicted by the thick green line. In these intervals the 2:1 solution is a stable focus since the eigenvalues also satisfy the condition  $|\lambda_i| = \sqrt{Det(DP)} < 1$ .

If  $\Delta > 0$  and  $\min_{i=1,2}(\lambda_i) < -1$ , as in  $d < d_B$  ranges in Fig. 6(b), (d), (f), the period-T solution is an unstable node. The corresponding critical point B is a period doubling bifurcation. For the angles of incline  $\beta = \pi/2$  and  $\beta = \pi/3$  the stability behavior of the periodic motion is very similar revealing the predominance of node stability in the observed range of d and having critical points of the same type: B period doubling bifurcation,  $A_1$  node/focus inflection and  $A_2$  focus/node

**Table 1** Conditions for stability as obtained from the linear stability analysis and shown in Fig. 2, with, for example,  $d_{A_j}$  corresponding to the value of d at  $A_i$ .

Interval	Criteria	Stability
$d < d_B  d_B < d < d_{A_1}, d_{A_2} < d < d_{A_3},  d_{A_1} < d < d_{A_2}, d > d_{A_3}$	$\begin{array}{l} \Delta>0 \text{ and }  \lambda_i >1\\ \Delta>0 \text{ and }  \lambda_i <1\\ \Delta<0 \text{ and }  \lambda_i <1 \end{array}$	unstable node stable node stable focus

inflection. For smaller  $\beta$ , the qualitative behavior of the 2:1 solutions changes; specifically, grazing bifurcations drive the transition to 3:1 solutions for larger values of d as compared with period doubling. We note that grazing bifurcations of the 2:1/pT solutions are observed for larger values of  $\beta$  as well. They are not shown here since they occur for values of  $d < d_B$  in those cases.

#### 4.2. The grazing transition and bistability

In addition to the conditions given in Table 1 above, recall that for smaller  $\beta$  the location of the period doubling bifurcation occurs at smaller d. Specifically, for  $\beta=\pi/6$  in the last row of Fig. 6, the linear stability analysis indicates an eigenvalue  $\lambda_1<-1$  for d<0.133. This stability result is represented by a change from solid to dashed line for the analytical solutions shown in Fig. 5(j)–(l). However, the linear stability analysis does not capture the grazing bifurcations indicated by the dash-dotted vertical lines in Fig. 5, which occurs for d>0.133. Then, in practice, the grazing bifurcation for d>0.133, rather than the local linearized behavior, drives the transition from 2:1 to 3:1 solutions. The values of d corresponding to grazing bifurcations are not included in Table 1, but instead discussed here.

For  $\beta=\pi/6$  we numerically detect a different type of critical point for the 2:1 solutions, namely, grazing bifurcations at which  $\dot{Z}_j=0$  and  $Z_j=d/2$  on the map  $P_2[46,47,49]$ . These are indicated by the vertical lines at  $d=G_1$  and  $d=G_2$  in Fig. 5(j)–(l), at which  $\dot{Z}_j=0$  and  $Z_j=d/2[46,47,49]$ . Fig. 8 zooms in on the bifurcation branches near these values. At these values of d there are transitions between 2:1 and 3:1 motions. The transition from 2:1 to 3:1 behavior at  $d=G_1$  is illustrated by the phase portrait and time series in Fig. 7. The initial conditions for these numerical simulations are obtained from the analytical expressions (27)–(30). In Fig. 7(d) the transition  $P_2$  takes the form of a loop in the  $\dot{Z}$  vs. Z phase plane. As d decreases, the loop intersects with Z=d/2, corresponding to an impact on  $\partial B$  with  $\dot{Z}_j=0$ . For decreasing d this additional impact persists as shown in Fig. 7(d), yielding 3:1 solutions with an additional  $P_1$  transition prior to  $P_2$ .

Fig. 8 compares the grazing bifurcation at  $d = G_1$  with the grazing bifurcation that occurs as d increases, leading to a transition from 3:1 to 2:1 solutions at  $d = G_2$ . Fig. 8(a)–(c) shows the branches for only one 3:1 solution: for increasing d, it exhibits grazing at  $G_2$ , at which  $\dot{Z}_k = 0$  and  $Z_k = d/2$  on the second  $P_1$ map. Fig. 8 does not show the branches for the 3:1 solution that we might expect to observe, born from grazing behavior at  $G_1(\dot{Z}_k = 0)$  and  $G_2(\dot{Z}_k = 0)$  on the map  $G_2(\dot{Z}_k = 0)$  and  $G_2(\dot{Z}_k = 0)$  on the map  $G_2(\dot{Z}_k = 0)$  on the ma

The phase plane behavior for  $d=G_1$  and  $d=G_2$  are in panels (d) and (g), respectively. In addition, the bi-stability of 3:1 and 2:1 solutions for  $G_1 < d < G_2$  is shown via the bifurcation branches of  $\dot{Z}_k, \varphi_k$  and  $\Delta t_k$ , as well as via the different phase plane behaviors at the value d=.14 in this bistable region. While [57] in chapter 6 explores some conditions for grazing and sticking and asymmetric behavior in the case with  $\beta=0$ , in general this bi-stability of different n:1 solutions via grazing has not been explored there or in other contexts.

While not the focus of this paper, these results illustrate the importance of grazing bifurcations in driving different types of transitions in the VI-EH, as well as for the potential for hysteresis between bistable behaviors. The analysis of grazing bifurcations for the VI-EH, as well as studying parameteric influence on the relative location of different types of bifurcations, is left for future investigation.

## 5. Energy output

Here we investigate the output voltage of the 2:1 behavior and compare these results with the 1:1 motion published in Serdukova et al. [59]. Three variables corresponding to output voltage are shown, output voltage  $U_k - U_{\rm in}$  at the  $k^{\rm th}$  impact, average output per impact  $\overline{U}_I$ , and averaged output per unit of time  $\overline{U}_T$ . The derivation of  $U_k - U_{\rm in}$  is summarized in Yurchenko et al. [58] and  $\overline{U}_I, \overline{U}_T$  are defined as

$$\overline{U}_{I} = \frac{\sum_{k=1}^{N} (U_{k} - U_{in})}{N}, \qquad \overline{U}_{T} = \frac{\sum_{k=1}^{N} (U_{k} - U_{in})}{t_{f} - t_{0}}, \tag{35}$$

where N is the sample size of impacts and  $t_f - t_0 = \frac{\omega}{\pi} (\tau_f - \tau_0)$  is the corresponding non-dimensionalized time interval. We average over this time interval, since it is just a constant rescaling of the dimensionalized time interval, and then it is easy to compare  $\overline{U}_I$  and  $\overline{U}_T$  on the same plot.

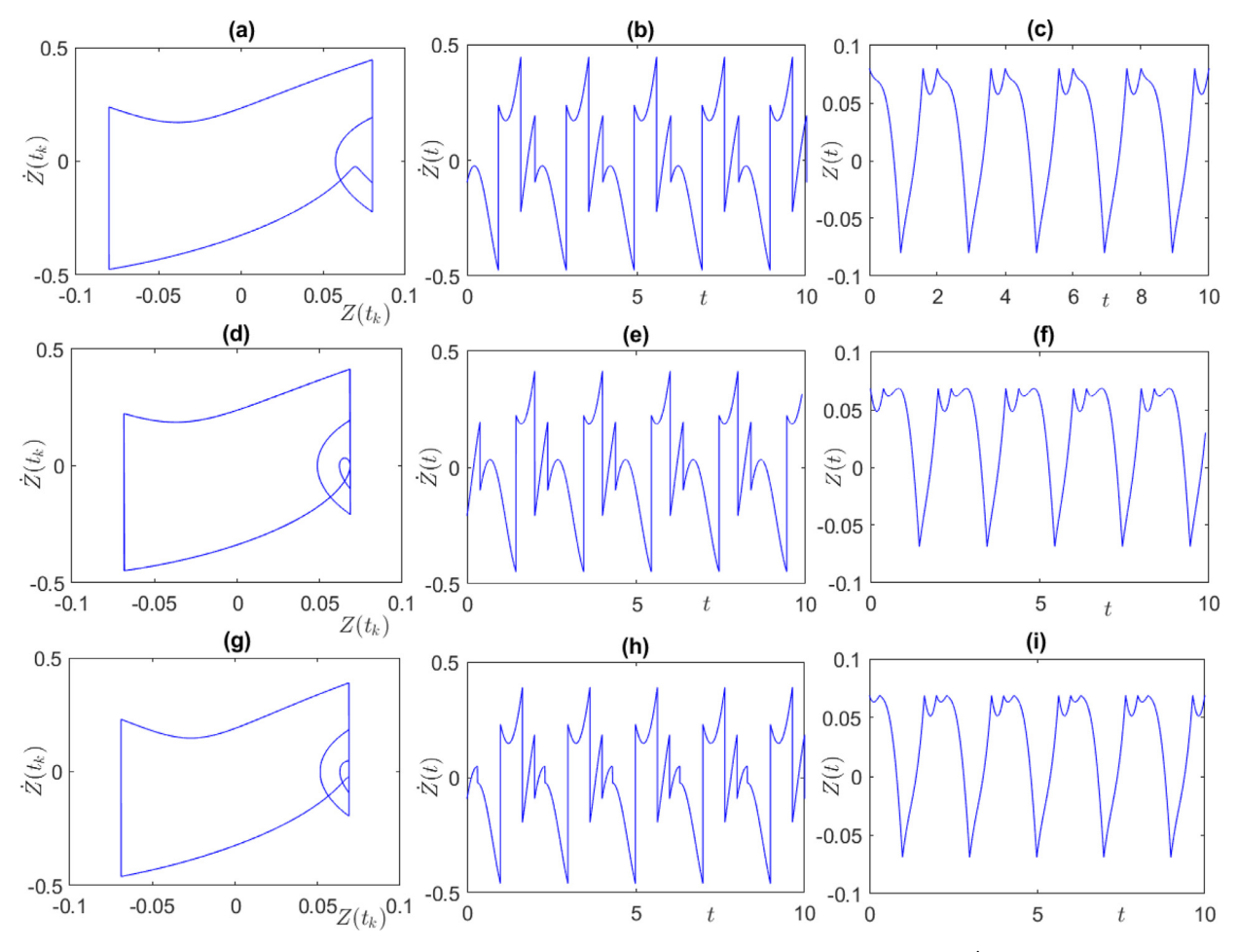


**Fig. 7.** Phase portrait and time series of period-*T* motion, with  $Z(t_0) = d/2$ . (a)–(c) 2:1 motion for d = 0.16, s = 0.27 m,  $\dot{Z}(t_0) = 0.1924, \varphi = 1.015$ ; (d)–(f) Grazing behavior of 2:1 motion for d = 0.1373, s = 0.2206 m,  $\dot{Z}(t_0) = 0.4149, \varphi = 5.840$ ; (g)–(i) (3:1) motion for d = 0.138, s = 0.23 m,  $\dot{Z}(t_0) = 0.1845, \varphi = 0.7342$ . For all figures  $\beta = \pi/6, M = 124.5$ g,  $r = 0.5, \|\hat{F}\| = 5$ N and  $\omega = 5\pi$  Hz.

Fig. 9 shows the output voltage for the 1:1 and 2:1 regimes, together with period doubled and chaotic regimes between these behaviors, for four different incline angles  $\beta$ . Panels (a)–(d) show variation due to cylinder length s with fixed strength of forcing  $\|\hat{F}\|$  and panels (e) and (f) show variations in  $\|\hat{F}\|$  with fixed s. One obvious difference is the trend in output voltage, as observed previously in Fig. 2. Away from bifurcations, the output voltage increases with both increasing  $\|F\|$  and increasing s. Then in (a)–(d)  $U_k$  decreases with s since s is proportional to s, while in (e) and (f) s shows a nonlinear increasing trend with decreasing s, due to the inverse relationship s0 in s1, as well as in the gravitational term s2.

The bifurcations in the motion also result in changes in the output voltage, which we discuss in terms of the different measures of averaged output voltage. For 1:1 periodic motion, the average energy per impact  $\overline{U}_I$  is equal to the average energy per unit of time  $\overline{U}_T$ , given that there are exactly two impacts for the 1:1 solutions. For the 1:1/pT, p>1 solutions, as well as for more complex and chaotic behavior as shown for smaller values of  $d>d_{\rm graz}$ , we see a slight increase in the rate of decrease with d of the average output voltage in (a)-(d), due primarily to the combination of values of impact velocities in the period doubled and more complex solutions that include some low velocity impacts. Following the transition to 2:1 motion for  $d < d_{\rm graz}$  the average energy outputs  $\overline{U}_I$  and  $\overline{U}_T$ show jumps in the output value. Averaged output per impact  $\overline{U}_I$  decreases due to the additional low velocity impact on  $\partial B$  in the period T=2 for 2:1 solution. For the same reason,  $\overline{U}_T$  increases due to this additional impact per period of the forcing. Similarly, for the transition from 2:1 solutions to 3:1 solutions, the additional low velocity impact results in jumps both in  $U_I$ , which decreases across this critical value of d, and in  $U_T$ , which increases across this critical transition. Note that here we show the grazing transition only at  $d=G_1$  for 2:1 to 3:1 solutions, corresponding to decreasing d in producing the bifurcation branches.

We also observe differences in the output voltages for different angles  $\beta$  in terms of the location in d and sequence of period doubling bifurcations and complex or chaotic behavior, and for the value of d at which the transition to 2:1 solutions

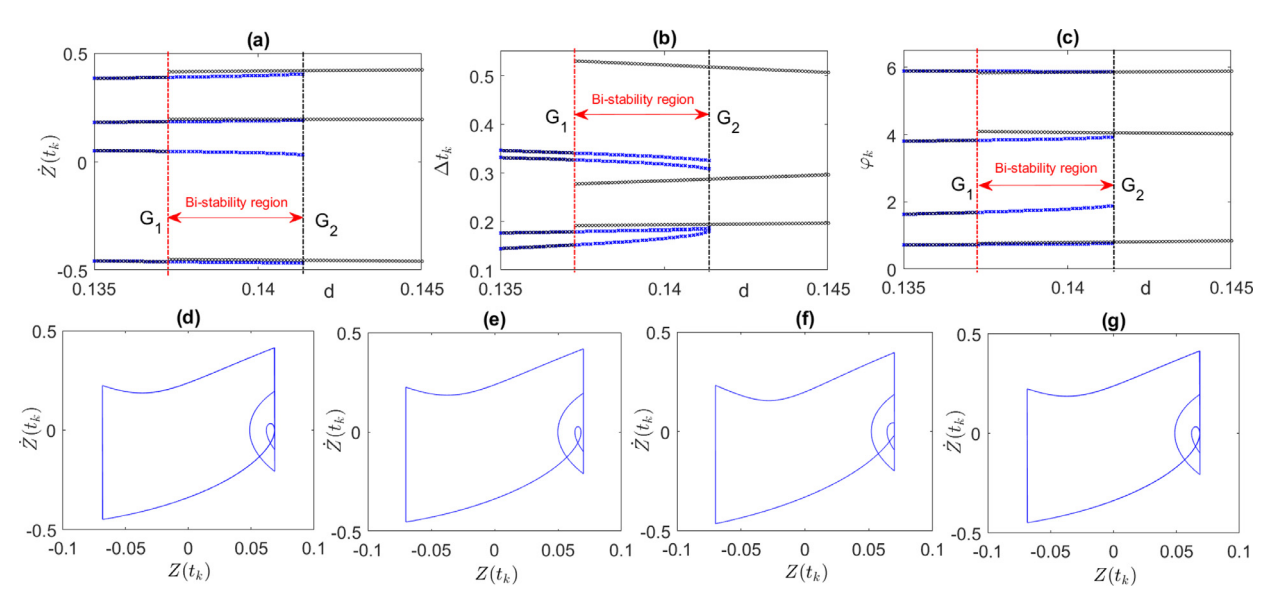


**Fig. 8.** Bi-stable behavior of periodic 2:1 (black open circles o's) and 3:1 (blue thin lines) solutions in the vicinity of the grazing bifurcation 0.1378 < d < 0.1419 for a)  $\dot{Z}_k$ , b)  $\varphi_k$ , c)  $\Delta t_k$ . Phase portraits with  $Z(t_0) = d/2$  for d) Grazing point  $G_1$  for  $\beta = \pi/6, d = 0.1373, s = 0.2206$  m,  $\dot{Z}(t_0) = 0.4149, \varphi = 5.840$ ; e) 2:1 motion for  $\beta = \pi/6, d = 0.14, s = 0.224$  m,  $\dot{Z}(t_0) = 0.4185, \varphi = 5.855$ ; f) 3:1 motion for  $\beta = \pi/6, d = 0.14, s = 0.224$  m,  $\dot{Z}(t_0) = 0.4985, \varphi = 5.864$ . (For interpretation of the references to color in this figure legend, the reader is referred to the web version of this article.)

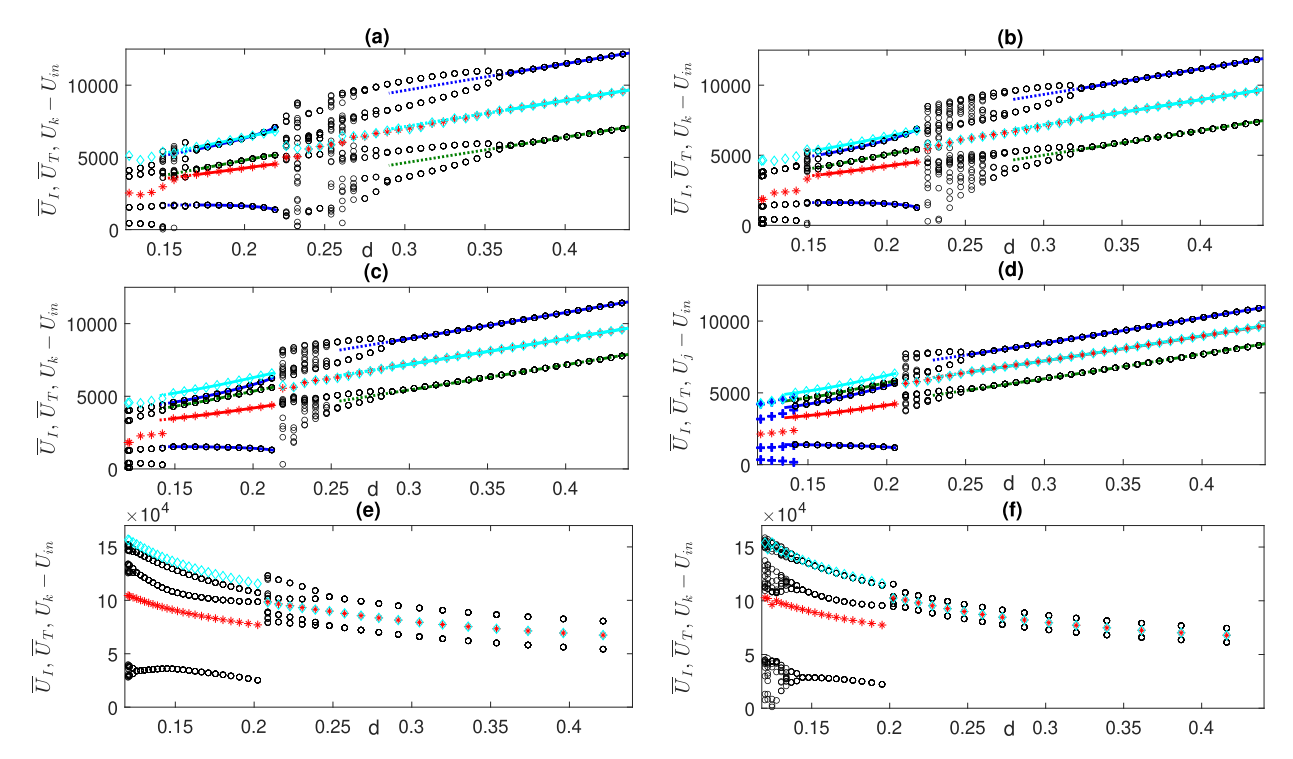


**Fig. 9.** Analytical results (solid, dash-dotted and dashed lines) and numerical simulations (open circles o's, stars \*'s and diamonds  $\diamondsuit$ 's) for output voltage  $\overline{U}_I$  (red) and  $\overline{U}_T$  (cyan) and  $U_k - U_{in}$  for (a)  $\beta = \pi/2$ ,0.19 < s < 0.72 m; (b)  $\beta = \pi/3$ ,0.19 < s < 0.72 m; (c)  $\beta = \pi/4$ ,0.19 < s < 0.72 m; (d)  $\beta = \pi/6$ ,0.19 < s < 0.72 m. For 2:1 solutions, in (a)–(c) the transitions  $P_3$ ,  $P_2$ ,  $P_1$  are located from top to bottom, while in (d),  $P_2$ ,  $P_3$ ,  $P_1$  are located from top to bottom. (e) For  $\beta = \pi/2$ , s = 0.85 m with varying  $\|\hat{F}\|$  between 6 N and 22 N. For all figures M = 124.5g,  $P_1 = 0.5$ ,  $\omega = 5\pi$  Hz. (For interpretation of the references to color in this figure legend, the reader is referred to the web version of this article.)

occurs. In general, as  $\beta$  increases, so do both the value of d at which period doubling of the 1:1 solution occurs, and the value of  $d_{\rm graz}$ , the maximum value for 2:1 solutions. Comparing Panels (a)-(d), for which d decreases with s, and Panels (e)-(f), for which d decreases with increasing  $\|\hat{F}\|$ , we observe a larger range of d in (a)-(d) for period doubled and complex or chaotic behavior. This is partly due to the fact that even though d decreases with increasing  $\|\hat{F}\|$ , the coefficient  $\bar{g}$  also decreases with increasing  $\|\hat{F}\|$ . Then for (e)-(f) as d decreases there is a reduced influence of gravity, which would otherwise generate period doubled and complex behavior. For the transition from 2:1 solutions to 2:1/pT behavior, we observe different trends, namely, that period doubling occurs for larger d for decreasing s, while it occurs for smaller s for increasing s in s in s in s in s increasing s in s in s increasing in s i

The result of this investigation suggests that the choice of the most efficient dynamical regime/device design in terms of the harvested electrical energy depends on the choice of measure for average output voltage and the changes in the parameter values of the system and the forcing. Our results illustrate some parametric dependencies connected to the relative location of period doubling, chaotic and grazing bifurcations.

#### 6. Conclusions

In this paper we determine semi-analytical solutions and stability conditions for the 2:1 motion of an inclined vibroimpacting energy harvester. These results also provide insight into the VI-EH's energy harvesting potential. The device is composed of a ball moving in a cylinder with dielectric elastomer material at the cylinder ends. It is driven by a harmonic forcing with period T, and positioned with an incline angle  $\beta$ . Energy is generated through impacts of the ball with the DE material characterized by a restitution coefficient r. The device exhibits pT-periodic motions, denoted as n:m/pT, where n(m)indicates the number of impacts of the ball, per period T, with the DE material on the bottom of the cylinder  $\partial B$  (top of the cylinder  $\partial T$ ). We develop a new generalized semi-analytical approach for analysis of n:1 periodic behavior, demonstrated for the 2:1 case, which provides parametric conditions for this behavior. Semi-analytical expressions for the generic period-Tmotion are derived through the three nonlinear maps that map the motion between the 3 impacts in the 2:1 motion per period. These maps, together with conditions that capture jump discontinuities in the velocity at impact, yield quadruples for the impact velocity, phase shift at impact, and time intervals between the impacts. This approach is particularly valuable given the nature of the transitions to 2:1 motion from 1:1/pT motion (or nearby chaotic behavior), since these behaviors are too complex to provide a basis for practical analytical representations that describe the onset of 2:1 motion. We show that the semi-analytical results for the 2:1 motion provide conditions for this onset, which we illustrate over ranges of parameters related to device length, forcing strength, and angle of incline.

Similar to [57] and [59], our derivation of this approach is based on a series of maps for a sequence of impacts, but we move beyond these earlier methods with a new generalizable approach that avoids the cumbersome calculations previously used to get explicit expressions. The analytical solutions are in excellent agreement with the numerical ones. Bifurcation points are obtained from a linear stability analysis around the asymmetric 2:1 periodic solutions, from which we conclude:

- 1. For larger values of the incline angle  $\beta$ , the stability behavior of the 2:1 periodic motion exhibits predominance of node stability in the observed range of d. These solutions lose stability through period doubling bifurcation for smaller values of d. This behavior is illustrated for  $\beta = \pi/2$ ,  $\beta = \pi/3$  and  $\beta = \pi/4$ .
- 2. For smaller values of incline  $\beta$ , the transition from 2:1 periodic behavior to 3:1 periodic behavior was observed as d decreases. This transition occurs via a grazing bifurcation that is numerically detected. It occurs for larger values of d as compared with the values for period doubling predicted by the linear analysis. These results are illustrated for  $\beta = \pi/6$ .
  - We also obtain analytical results for the energy output for 1:1 and 2:1 motions, based on the existence and stability results. We can then compare and identify the most energetically efficient operating mode of the harvester, comparing analytical results with numerical simulations for additional motions, including 1:1/pT and 3:1. We observe that:
- 3. The n:1 periodic asymmetric motions for n > 1 are less efficient compared to the motion with 1:1 alternating top and bottom impacts per period of the forcing, when measured in terms of converted electrical energy per impact.
- 4. The 2:1 periodic motion results in significant differences between the two measures of the harvested energy, averaged per impact,  $U_I$ , and averaged over time interval,  $U_T$ , giving greater value for  $U_T$ . Similar observations for 3:1 behavior are also shown.
  - The comparisons with computations reveal additional unexplored phenomena, particularly in the case of smaller  $\beta$ , not previously documented in the dynamics of such a system.
- 5. In the case of  $\beta = \pi/6$ , we observe bi-stability of 2:1 motion and 3:1 motion, with two different grazing transitions between these behaviors. Our preliminary results (comparing Figs. 2 and 4) also suggest that for smaller r, we expect to see an increased prevalence of grazing bifurcations, transitions from n:1 to (n+1):1, in contrast to period doubling bifurcations, transitions from n:1 to n:1/pT, p > 1 solutions.

The analytical results presented here for transitions to 2:1 behavior show important differences in the change of energy output associated with different types of bifurcations - e.g. period doubling vs. grazing bifurcations. While we focus here on the influence of the parameters  $\beta$  and d on energy output, the preliminary results shown for bi-stability and the influence of

r indicate important areas for further exploration. The analysis developed here provides a necessary foundation for further exploration in these directions.

## **Declaration of Competing Interest**

The authors declare that they have no known competing financial interests or personal relationships that could have appeared to influence the work reported in this paper.

### **CRediT authorship contribution statement**

**Larissa Serdukova:** Methodology, Software, Writing - original draft, Writing - review & editing. **Rachel Kuske:** Conceptualization, Methodology, Validation, Writing - review & editing. **Daniil Yurchenko:** Conceptualization, Methodology, Validation, Writing - review & editing.

# Acknowledgments

The authors gratefully acknowledge partial funding for this work from NSF Division CMMI 2009270 and EPSRC EP/V034391/1.

#### Appendix A.

Here we give the details for the calculations of the eigenvalues  $\lambda_{1,2}$ . The entries in the matrices in (33)are

$$\frac{\partial t_{k+1}}{\partial t_k} = \frac{r\dot{Z}_k - \tilde{g}T_1 - f(t_k)T_1}{r\dot{Z}_k - \tilde{g}T_1 - F_1(t_{k+1}) + F_1(t_k)}, 
\frac{\partial t_{k+1}}{\partial \dot{Z}_k} = \frac{-rT_1}{r\dot{Z}_k - \tilde{g}T_1 - F_1(t_{k+1}) + F_1(t_k)}, 
\frac{\partial \dot{Z}_{k+1}}{\partial t_k} = \frac{\partial t_{k+1}}{\partial t_k} [f(t_{k+1}) + \tilde{g}] - [f(t_k) + \tilde{g}], 
\frac{\partial \dot{Z}_{k+1}}{\partial \dot{Z}_k} = -r + \frac{\partial t_{k+1}}{\partial \dot{Z}_k} [f(t_{k+1}) + \tilde{g}], 
\frac{\partial t_{k+2}}{\partial t_{k+1}} = \frac{r\dot{Z}_{k+1} - \tilde{g}T_2 - f(t_{k+1})T_2}{r\dot{Z}_{k+1} - \tilde{g}T_2 - F_1(t_{k+2}) + F_1(t_{k+1})}, 
\frac{\partial t_{k+2}}{\partial \dot{Z}_{k+1}} = \frac{-rT_2}{r\dot{Z}_{k+1} - \tilde{g}T_2 - F_1(t_{k+2}) + F_1(t_{k+1})}, 
\frac{\partial \dot{Z}_{k+2}}{\partial \dot{Z}_{k+1}} = \frac{\partial t_{k+2}}{\partial t_{k+1}} [f(t_{k+2}) + \tilde{g}] - [f(t_{k+1}) + \tilde{g}]. 
\frac{\partial \dot{Z}_{k+2}}{\partial t_{k+1}} = -r + \frac{\partial t_{k+2}}{\partial \dot{Z}_{k+1}} [f(t_{k+2}) + \tilde{g}],$$
(A.2)

and

$$\frac{\partial t_{k+3}}{\partial t_{k+2}} = \frac{r\dot{Z}_{k+2} - \bar{g}T_3 - f(t_{k+2})T_3}{r\dot{Z}_{k+2} - \bar{g}T_3 - F_1(t_{k+3}) + F_1(t_{k+2})},$$

$$\frac{\partial t_{k+3}}{\partial \dot{Z}_{k+2}} = \frac{-rT_3}{r\dot{Z}_{k+2} - \bar{g}T_3 - F_1(t_{k+3}) + F_1(t_{k+2})},$$

$$\frac{\partial \dot{Z}_{k+3}}{\partial t_{k+2}} = \frac{\partial t_{k+3}}{\partial t_{k+2}} [f(t_{k+3}) + \bar{g}] - [f(t_{k+2}) + \bar{g}],$$

$$\frac{\partial \dot{Z}_{k+3}}{\partial \dot{Z}_{k+2}} = -r + \frac{\partial t_{k+3}}{\partial \dot{Z}_{k+2}} [f(t_{k+3}) + \bar{g}].$$
(A.3)

For the period-T motion the trace of the linearized matrix DP is

$$Tr(DP) = -\frac{r^6 \dot{Z}(t_k)}{F_1(t_{k+2}) - F_1(t_{k+3}) - rF_1(t_{k+1}) + rF_1(t_{k+2}) + r^2 F_1(t_k) - r^2 F_1(t_{k+1}) + \sigma_1},$$
(A.4)

where  $\sigma_1 = r^3 \dot{Z}(t_k) - \bar{g}T_3 + r\bar{g}T_2 - r^2\bar{g}T_1$ . The determinant of the linearized matrix *DP* is a nonlinear function of  $r.\bar{g}.\dot{Z}(t_k).T_1.T_2.T_3.f(t_k).f(t_{k+1}).f(t_{k+2}).f(t_{k+3}).F_1(t_k).F_1(t_{k+1}).F_1(t_{k+2})$  and  $F_1(t_{k+3}).$ 

#### References

- [1] B. Yang, H. Liu, J. Liu, C. Lee, Micro and nano energy harvesting technologies, Published by Artech House, 2014 ISBN 10: 1608078140, ISBN 13: 9781608078141.
- [2] N. Stephen, On energy harvesting from ambient vibration, J. Sound Vib. 293 (1-2) (2006) 409-425, doi:10.1016/j.jsv.2005.10.003.
- [3] C.R. Bowen, V.Y. Topolov, H.A. Kim, Modern Piezoelectric Energy-Harvesting Materials, Springer Series in Materials Science, 238, Springer International Publishing, Cham, 2016, doi:10.1007/978-3-319-29143-7.
- [4] D. Briand, E. Yeatman, S. Roundy, Micro Energy Harvesting, Advanced Micro and Nanosystems, Wiley-VCH Verlag GmbH & Co. KGaA, Weinheim, Germany, 2015, doi:10.1002/9783527672943.
- [5] N. Elvin, A. Erturk, Advances in Energy Harvesting Methods, Springer New York, New York, NY, 2013, doi:10.1007/978-1-4614-5705-3.
- [6] Y. Jia, J. Yan, K. Soga, A.A. Seshia, Parametric resonance for vibration energy harvesting with design techniques to passively reduce the initiation threshold amplitude, Smart Mater. Struct. 23 (6) (2014) 065011, doi:10.1088/0964-1726/23/6/065011.
- [7] R. Bobryk, D. Yurchenko, Enhancing energy harvesting by a linear stochastic oscillator, Probab. Eng. Mech. 43 (2016) 1–4, doi:10.1016/j.probengmech. 2015.10.007.
- [8] D. Yurchenko, P. Alevras, Parametric pendulum based wave energy converter, Mech. Syst. Signal Process. 99 (2018) 504–515, doi:10.1016/j.ymssp.2017. 06.026.
- [9] M. Wiercigroch, A. Najdecka, V. Vaziri, Nonlinear dynamics of pendulums system for energy harvesting, in: Springer Proceedings in Physics, 2011, pp. 35–42, doi:10.1007/978-94-007-2069-5\_4.
- [10] K. Yerrapragada, M.H. Ansari, M.A. Karami, Enhancing power generation of floating wave power generators by utilization of nonlinear roll-pitch coupling, Smart Mater. Struct. 26 (9) (2017) 094003, doi:10.1088/1361-665X/aa7710.
- [11] Y. Kuang, M. Zhu, Parametrically excited nonlinear magnetic rolling pendulum for broadband energy harvesting, Appl. Phys. Lett. 114 (20) (2019) 203903, doi:10.1063/1.5097552.
- [12] K. Kecik, M. Borowiec, An autoparametric energy harvester, Eur. Phys. J. Spec. Top. 222 (7) (2013) 1597-1605, doi:10.1140/epjst/e2013-01948-2.
- [13] R.V. Bobryk, D. Yurchenko, On enhancement of vibration-based energy harvesting by a random parametric excitation, J. Sound Vib. 366 (2016) 407–417, doi:10.1016/j.jsv.2015.11.033.
- [14] F.E. Dotti, M.D. Sosa, Pendulum systems for harvesting vibration energy from railroad tracks and sleepers during the passage of a high-speed train: afeasibility evaluation, Theor. Appl. Mech. Lett. 9 (4) (2019) 229–235, doi:10.1016/j.taml.2019.03.005.
- [15] R.H. Avanço, A.M. Tusset, M. Suetake, H.A. Navarro, J.M. Balthazar, A. Nabarrete, Energy harvesting through pendulum motion and DC generators, Latin Am. I. Solids Struct. 16 (1) (2019). doi:10.1590/1679-78255013.
- [16] D.D. Quinn, A.L. Triplett, A.F. Vakakis, L.A. Bergman, Energy harvesting from impulsive loads using intentional essential nonlinearities, J. Vib. Acoust. 133 (1) (2011), doi:10.1115/1.4002787.
- [17] P. Green, K. Worden, K. Atallah, N. Sims, The benefits of Duffing-type nonlinearities and electrical optimisation of a mono-stable energy harvester under white Gaussian excitations, J. Sound Vib. 331 (20) (2012) 4504–4517, doi:10.1016/j.jsv.2012.04.035.
- [18] M.F. Daqaq, R. Masana, A. Erturk, D. Dane Quinn, On the role of nonlinearities in vibratory energy harvesting: a critical review and discussion, Appl. Mech. Rev. 66 (4) (2014), doi:10.1115/1.4026278.
- [19] N. Lingala, N. Sri Namachchivaya, I. Pavlyukevich, H.C. Yeong, Periodically Forced Noisy Mathieu-Duffing-Van der Pol Oscillator: From Energy Harvesting to Stochastic Resonance, Technical Report.
- [20] Z. Ghouli, M. Hamdi, F. Lakrad, M. Belhaq, Quasiperiodic energy harvesting in a forced and delayed Duffing harvester device, J. Sound Vib. 407 (2017) 271–285, doi:10.1016/j.jsv.2017.07.005.
- [21] H.T. Zhu, Probabilistic solution of a Duffing-type energy harvester system under Gaussian white noise, ASCE-ASME J. Risk Uncert Eng. Syst. Part B 1 (1) (2015), doi:10.1115/1.4029143.
- [22] G. Sebald, H. Kuwano, D. Guyomar, B. Ducharne, Experimental Duffing oscillator for broadband piezoelectric energy harvesting, Smart Mater. Struct. 20 (10) (2011) 102001, doi:10.1088/0964-1726/20/10/102001.
- [23] S.P. Pellegrini, N. Tolou, M. Schenk, J.L. Herder, Bistable vibration energy harvesters: a review, J. Intell. Mater. Syst. Struct. 24 (11) (2013) 1303–1312, doi:10.1177/1045389X12444940.
- [24] Y. Gao, Y. Leng, A. Javey, D. Tan, J. Liu, S. Fan, Z. Lai, Theoretical and applied research on bistable dual-piezoelectric-cantilever vibration energy harvesting toward realistic ambience, Smart Mater. Struct. 25 (11) (2016) 115032, doi:10.1088/0964-1726/25/11/115032.
- [25] H. Fu, E.M. Yeatman, Rotational energy harvesting using bi-stability and frequency up-conversion for low-power sensing applications: theoretical
- modelling and experimental validation, Mech. Syst. Signal Process. 125 (2019) 229–244, doi:10.1016/j.ymssp.2018.04.043.
  [26] D. Hawes, R. Langley, Limits on the power available to harvest from broadband random excitation, J. Sound Vib. 399 (2017) 244–256, doi:10.1016/j.jsv.
- 2017.03.036.
  [27] S. Zhou, L. Zuo, Nonlinear dynamic analysis of asymmetric tristable energy harvesters for enhanced energy harvesting, Commun. Nonlinear Sci. Numer. Simul. 61 (2018) 271–284, doi:10.1016/j.cnsns.2018.02.017.
- [28] D. Huang, S. Zhou, G. Litak, Analytical analysis of the vibrational tristable energy harvester with a RL resonant circuit, Nonlinear Dyn. 97 (1) (2019) 663–677, doi:10.1007/s11071-019-05005-6.
- [29] H. Deng, Y. Du, Z. Wang, J. Ye, J. Zhang, M. Ma, X. Zhong, Poly-stable energy harvesting based on synergetic multistable vibration, Commun. Phys. 2 (1) (2019) 21, doi:10.1038/s42005-019-0117-9.
- [30] T. Yang, Q. Cao, Novel multi-stable energy harvester by exploring the benefits of geometric nonlinearity, J. Stat. Mech 2019 (3) (2019) 033405, doi:10.
- [31] A. Abdelkefi, A.H. Nayfeh, M.R. Hajj, Modeling and analysis of piezoaeroelastic energy harvesters, Nonlinear Dyn. 67 (2) (2012) 925–939, doi:10.1007/s11071-011-0035-1.
- [32] S. Orrego, K. Shoele, A. Ruas, K. Doran, B. Caggiano, R. Mittal, S.H. Kang, Harvesting ambient wind energy with an inverted piezoelectric flag, Appl. Energy 194 (2017) 212–222, doi:10.1016/j.apenergy.2017.03.016.
- [33] J. Wang, G. Li, S. Zhou, G. Litak, Enhancing wind energy harvesting using passive turbulence control devices, Appl. Sci. 9 (5) (2019) 998, doi:10.3390/app9050998.
- [34] J. Wang, S. Zhou, Z. Zhang, D. Yurchenko, High-performance piezoelectric wind energy harvester with Y-shaped attachments, Energy Convers. Manag. 181 (2019) 645–652, doi:10.1016/j.enconman.2018.12.034.
- [35] Z. Jin, G. Li, J. Wang, Z. Zhang, Design, modeling, and experiments of the vortex-induced vibration piezoelectric energy harvester with bionic attachments, Complexity 2019 (2019) 1–13, doi:10.1155/2019/1670284.
- [36] J. Wang, L. Geng, L. Ding, H. Zhu, D. Yurchenko, The state-of-the-art review on energy harvesting from flow-induced vibrations, Appl. Energy 267 (2020) 114902, doi:10.1016/j.apenergy.2020.114902.
- [37] R.A. Ibrahim, Vibro-impact dynamics: modeling, mapping and applications, Lect. Notes Appl. Comput. Mech. (2009).
- [38] M.F. Dimentberg, D.V. lourtchenko, Random vibrations with impacts: a review, Nonlinear Dyn. 36 (2-4) (2004) 229–254, doi:10.1023/B:NODY. 0000045510.93602.ca.
- [39] A.B. Nordmark, Universal limit mapping in grazing bifurcations, Phys. Rev. E 55 (1) (1997) 266-270, doi:10.1103/PhysRevE.55.266.
- [40] F. Peterka, A. Tondl, Phenomena of subharmonic motions of oscillator with soft impacts, Chaos Solitons Fractals 19 (5) (2004) 1283–1290, doi:10.1016/S0960-0779(03)00335-7.
- [41] F. Peterka, T. Kotera, S. Čipera, Explanation of appearance and characteristics of intermittency chaos of the impact oscillator, Chaos Solitons Fractals 19 (5) (2004) 1251–1259, doi:10.1016/S0960-0779(03)00327-8.

- [42] A. Rounak, S. Gupta, Bifurcations in a pre-stressed, harmonically excited, vibro-impact oscillator at subharmonic resonances, Int. J. Bifurc. Chaos 30 (08) (2020).
- [43] D.R.J. Chillingworth, Discontinuity geometry for an impact oscillator, Dyn. Syst. 17 (4) (2002) 389-420, doi:10.1080/1468936021000041654.
- [44] D.J. Wagg, S.R. Bishop, Dynamics of a two degree of freedom vibro-impact system with multiple motion limiting constraints, Int. J. Bifurc. Chaos 14 (01) (2004) 119–140, doi:10.1142/S0218127404009223.
- [45] D. Wagg, Periodic sticking motion in a two-degree-of-freedom impact oscillator, Int. J. Non Linear Mech. 40 (8) (2005) 1076–1087, doi:10.1016/j.
- [46] M. Di Bernardo, C.J. Budd, A.R. Champneys, P. Kowalczyk, Piecewise-smooth Dynamical Systems, Applied Mathematical Sciences, 163, Springer London, London, 2008, doi:10.1007/978-1-84628-708-4.
- [47] D.J.W. Simpson, S.J. Hogan, R. Kuske, Stochastic regular grazing bifurcations, SIAM J. Appl. Dyn. Syst. 12 (2) (2013) 533-559, doi:10.1137/120884286.
- [48] P. Kumar, S. Narayanan, S. Gupta, Stochastic bifurcations in a vibro-impact Duffing-Van der Pol oscillator, Nonlinear Dyn. 85 (1) (2016) 439–452, doi:10.1007/s11071-016-2697-1.
- [49] D.J.W. Simpson, R. Kuske, The influence of localized randomness on regular grazing bifurcations with applications to impacting dynamics, J. Vib. Control 24 (2) (2018) 407–426, doi:10.1177/1077546316642054.
- [50] S. Shaw, P. Holmes, A periodically forced piecewise linear oscillator, J. Sound Vib. 90 (1) (1983) 129–155, doi:10.1016/0022-460X(83)90407-8.
- [51] A. El Aroudi, H. Ouakad, L. Benadero, M. Younis, Analysis of bifurcation behavior of a piecewise linear vibrator with electromagnetic coupling for energy harvesting applications, Int. J. Bifurc. Chaos 24 (05) (2014) 1450066, doi:10.1142/S0218127414500667.
- [52] M. Borowiec, G. Litak, S. Lenci, Noise effected energy harvesting in a beam with stopper, Int. J. Struct. Stab. Dyn. 14 (08) (2014) 1440020, doi:10.1142/S0219455414400203.
- [53] O. Gendelman, A. Alloni, Dynamics of forced system with vibro-impact energy sink, J. Sound Vib. 358 (2015) 301-314, doi:10.1016/j.jsv.2015.08.020.
- [54] B.D. Truong, C. Phu Le, E. Halvorsen, Power optimization and effective stiffness for a vibration energy harvester with displacement constraints, J. Micromech. Microeng, 26 (12) (2016) 124006, doi:10.1088/0960-1317/26/12/124006.
- [55] M. Bendame, E. Abdel-Rahman, M. Soliman, Wideband, low-frequency springless vibration energy harvesters: part I, J. Micromech. Microeng. 26 (11) (2016) 115021, doi:10.1088/0960-1317/26/11/115021.
- [56] B. Guo, Y. Liu, R. Birler, S. Prasad, Self-propelled capsule endoscopy for small-bowel examination: proof-of-concept and model verification, Int. J. Mech. Sci. 174 (2020) 105506, doi:10.1016/j.ijmecsci.2020.105506.
- [57] A.C.J. Luo, Y. Guo, Vibro-Impact Dynamics, John Wiley & Sons Ltd, Oxford, UK, 2013, doi:10.1002/9781118402924.
- [58] D. Yurchenko, Z. Lai, G. Thomson, D. Val, R. Bobryk, Parametric study of a novel vibro-impact energy harvesting system with dielectric elastomer, Appl. Energy 208 (2017) 456–470, doi:10.1016/j.apenergy.2017.10.006.
- [59] L. Serdukova, R. Kuske, D. Yurchenko, Stability and bifurcation analysis of the period-T motion of a vibroimpact energy harvester, Nonlinear Dyn. 98 (3) (2019) 1807–1819, doi:10.1007/s11071-019-05289-8.
- [60] A.C. Luo, Period-doubling induced chaotic motion in the LR model of a horizontal impact oscillator, Chaos Solitons Fractals 19 (4) (2004) 823–839, doi:10.1016/S0960-0779(03)00195-4.